JOURNAL OF GEOPHYSICAL RESEARCH, VOL. 95, NO. C6, PAGES 9585–9610, JUNE 15, 1990

Experimental Observations of Baroclinic Eddies on a Sloping Bottom

JOHN A. WHITEHEAD

Physical Oceanography Department, Woods Hole Oceanographic Institution, Woods Hole, Massachusetts

MELVIN E. STERN

Department of Oceanography, Florida State University, Tallahassee, Florida

GLENN R. FLIERL AND BARRY A. KLINGER

Earth, Atmospheric and Planetary Sciences, Massachusetts Institute of Technology, Cambridge, Massachusetts

Baroclinic eddies in a rotating box with a sloping bottom were produced by squirting dense salt water up the sloping bottom and along the "eastern" wall. The jet stagnated in shallow water and was ejected normal to the wall. For certain parameters (volume flux of jet, etc.), a coherent lens of dense bottom water formed and propagated west with an overlying cyclonic vortex. The circulation in the bottom lens, on the other hand, was relatively weak. No such eddy forms when the depth of fresh water is relatively deep, and a regime diagram is given for the formation of the coherent eddies. Thus a relatively simple structure emerges despite the complexity of the generating process. The pressure field determined from density measurements is discussed in terms of an integral theorem for coherent eddies, and the westward propagation is also related to previous theories. Several other techniques for generating such eddies are discussed.

1. INTRODUCTION

Isolated eddies are some of the most beautiful structures in fluid mechanics to observe experimentally, with the ring vortex and a vortex pair in a homogeneous fluid being two simple examples. The vortex pair became of interest in geophysical fluid dynamics when *Stern* [1975] found a class of vortex pair solutions for flow in a rotating fluid and, in particular, on the β plane. The original eddy pairs, which have come to be called "modons," had rather special properties. For instance, they were found to propagate eastward in the presence of the β effect [*Larichev and Reznik*, 1976*b*] and to not radiate Rossby waves. Theoretical works since have considerably broadened the types and properties of modon eddies in rotating fluids [*Larichev and Reznik*, 1976*a*, *b*; *Flierl*, 1979*a*, *b*, 1984; *Flierl et al.*, 1980, 1983; *Boyd*, 1981; *Zabusky and McWilliams*, 1982; *Nof*, 1983; *Mory*, 1985] including baroclinic modons which have vortices of opposite sign stacked vertically and cold eddies on a sloping bottom.

Isolated eddies have been extensively observed in the ocean and in the Earth's and other planetary atmospheres. *Malanotte-Rizzoli* [1982] cites the three best known ones: a Gulf Stream ring, Jupiter's Red Spot, and a blocking ridge eddy. In oceanography, there are a number of smaller eddies which have now been documented, often called "meddies," after the identification of a water parcel with clear Mediterranean origin off the Bahamas. The oceanic eddies have a number of features that are characteristic of isolated eddies and not characteristic of solitary waves such as strong local circulation, closed streamlines, and anomalous potential vorticity. They also move relative to their surroundings and carry trapped fluid with them. In spite of the numerous observations of these eddies in the ocean, and the numerous theories, there is at present no detailed connection between isolated eddy structures observed in the ocean and the modon solutions. There is, however, good correspondence between numerical computations and some modon solutions. Laboratory studies can serve as a bridge between the theories and computations and actual fluid flows in nature, as well as serving their time-honored role of being a direct test of calculations and suggesting new processes in which the eddies are actually generated.

This study concerns the origin and properties of a lens of salty water which lies over a sloping bottom in a rotating fluid, in a gravitational field, with a level upper surface. The geometry produces a topographic β plane with north onshore, south offshore, east to the right looking onshore and west to the left (see Figures 1 and 2). This configuration was originally suggested [*Nof*, 1983] by a model of an eddy of dense water on a sloping bottom which lay below a semi-infinite region of motionless water. The eddy was predicted to travel to the west with a characteristic velocity given by the formula $c = g^* S/f$. Here $g^* = g \, \Delta \rho/\rho$ is gravity multiplied by the relative density difference between the two fluids (often called reduced gravity), S is the slope of the bottom, and f is the Coriolis parameter. Water in the lens circulated anticyclonically, and the deep overlying fluid was motionless. Later experimental and theoretical studies by *Mory* [1983, 1985], and *Mory et al.* [1987] indicated that similar eddies can be produced in a laboratory turntable experiment but they possessed qualitative differences from the Nof solution. Instead of the fluid in the lens being anticyclonic, it was relatively motionless compared to the strong cyclonic circulation in the water over the eddy. In addition, a general pressure integral was derived, which depends only on the rapid decay of the upper layer velocity from the eddy center. It showed that most of the kinetic energy should be in the fluid above the dense lens.

It should be pointed out that the dynamics of dense eddies

Paper number 90JC03777.
0148-0227/90/89JC03777$5.00

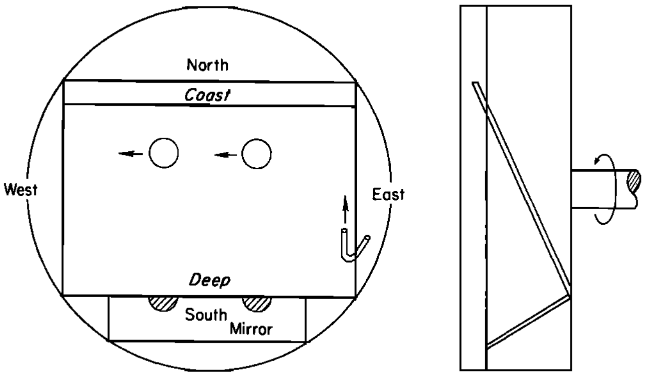

Fig. 1. Top and side view of the experimental apparatus to make eddies of dense water on a sloping bottom.

on a sloping bottom bear on the important process of deep water formation in the ocean. *Killworth* [1979] has pointed out the important role of cyclonic circulation in the surface layer during dense water formation, and some of the new methods of generating eddies which we relate here bear on this.

The purpose of this paper is to describe an experiment (section 2) which produces one or more eddies from an impulsively started source. Qualitatively (section 3), the eddies are very similar to those observed by *Mory et al.* [1987] in spite of the very different method of generation. We also demonstrate numerous other ways of making these eddies, since it is important in the context of the ocean problem to demonstrate that these simple eddies can arise from various kinds of generating processes which are less artificial (and less controlled!) than those in the *Mory et al.* [1987] experiment.

2. Eddies From a Coastal Jet

If one has a rotating fluid on a sloping bottom, so that a topographic β plane is produced; and if a source of dense water is squirted up the slope, the dense fluid will curve to the right (east) and continue to do so until it reaches its rest latitude; from there it will flow downhill and curve toward the west. There are two ways for this westward directed flow to continue. One way is for the water to collect as coherent eddies and propagate to the west in the manner indicated below. The second way, which we observed when the upper layer was very deep, was to form a downhill slumping of the dense fluid in a very broad and thin Ekman layer. The central result is that isolated eddies emerge from a general and rather nondescript process, which nevertheless has conditions that can set eddies up. This is a step beyond earlier experiments [*Mory*, 1983, *Mory et al.*, 1987] in which isolated eddies were generated by a more explicit condition, namely, dense fluid in a removable cylindrical wall.

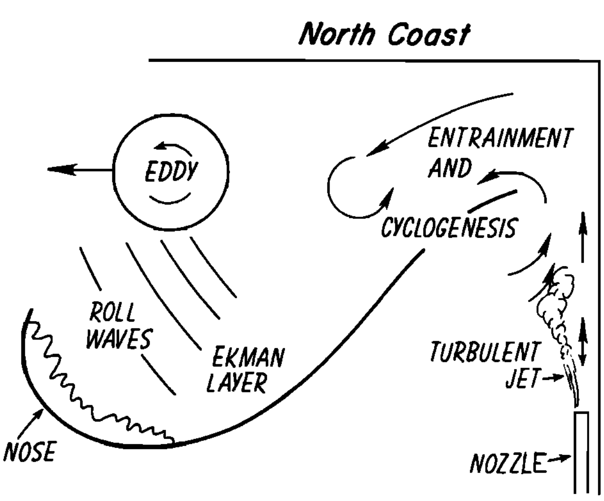

Fig. 2. Sketch of the processes in the eddy-generating region.

The experimental apparatus (sketched in Figure 1) consisted of a plywood false bottom mounted with a 1:5 slope on the two-meter rotating turntable at the Coastal Research Center of Woods Hole Oceanographic Institution. A grid of lines spaced 10 cm apart was painted onto a white background on the false bottom. The tank was filled to a maximum depth of 23 cm with fresh water. The intersection of the water with a sloping bottom (to be called the coast) corresponds to the northern shore of the topographic beta plane. East is to the right looking onshore, west is to the left, and south is at the deepest end, as shown in Figure 1. Vertical sidewalls were attached to the eastern and western boundaries of the false bottom.

A nozzle, made of 10 cm length of glass tubing of 0.76-cm internal diameter, was a source of intrusive fluid. It was connected by hose to a flow meter and from there to a reservoir filled with dyed salty water of density 1.012 g/cm^3 for the early runs and 1.031 g/cm^3 for the final runs. The source was located at a specified distance offshore next to the eastern wall and was pointed up the slope so that a turbulent jet of salty water squirted up the slope.

3. Qualitative Observations

The flow that resulted from the jet on the eastern wall was relatively complicated, so it is sketched in Figure 2. Salt water from the jet rose along the eastern coast and slowed down. It stagnated either at or near the coast and then slumped down the slope by gravitational acceleration. Meanwhile, it curved westward. Parts of the dyed fluid descended in a bottom Ekman layer, in which nonlinearities in the form of roll waves [*Chow*, 1959], or possibly waves due to Ekman layer instability, along with a distinct front were obvious. Above the Ekman layer the desired eddies formed for certain ranges of the controlled parameters.

A photograph of an excellent set of eddies is shown in Figure 3. Each eddy consisted of a circular lens of (dyed) salty water lying on the sloping bottom. The lens was roughly bell-shaped and approximately half as thick as the depth of the water. The eddies also had a number of features not visible in that photograph. The montage of streak photos in Figure 4 shows that a typical eddy travelled westward, with virtually no northward drift (in contrast to *Mory et al.* [1987]), and had a gyre of trapped cyclonically circulating fresh water immediately over the lens of salty water. Fluid in the gyre above the lens stayed trapped above the lens for the life of the eddy. This, along with the westward drift is revealed in Figure 5, which shows the motion of a floating pellet over an eddy.

The number and quality of the eddies varied as a function of the control parameters. A systematic set of runs was conducted to obtain a regime diagram in parameter

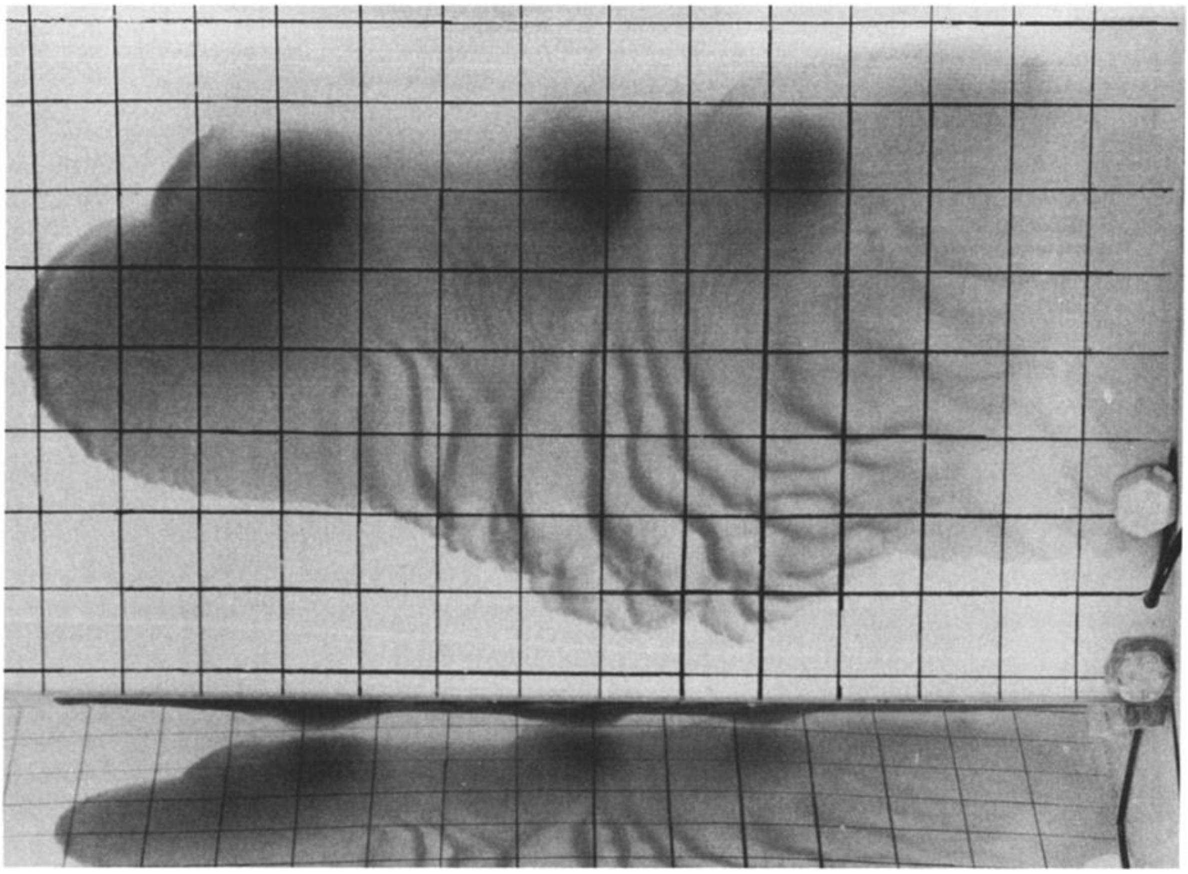

Fig. 3. A train of three baroclinic eddies of dyed salty water on a white gridded sloping bottom. The top of the photograph is the coast (which is north in this topographical β plane). The Ekman layer and roll waves bleed some fluid down the slope. The view in the bottom portion is an inverted elevation view through a mirror placed in the deep part of the tank at approximately 50°. The eddies all travel westward and have cyclonic circulation. Parametrically, this run is directly below the circled run in Figure 6.

space. For this set, turntable rotation was set to a period of 15.00 ± 0.1 s, and the duration of the jet was set at 30. The other two control parameters were speed of the jet and distance of the jet offshore, and these were systematically varied. Figure 6 shows the regime diagram from this set of experiments. It shows that there were a number of regions with vastly different flows. When the jet was very weak and far offshore, no eddy formed and the jet plunged down the slope as a gravity current. Photographs of this case, denoted 0 in Figure 6, are shown in Figure 7. For stronger forcing, denoted by F in Figure 6, there was a sharp front or nose along the left-hand bottom of the Ekman layer. The nose was approximately 2 to 3 times the Ekman layer thickness and gave every appearance of being very similar to the nose of a nonrotating frictional density current. It is interesting for its own sake, but is beyond the scope of the present study. When the jet was even closer to shore or was made stronger, one eddy formed as denoted by a number 1 in Figure 6. This eddy has already been described. For an even stronger jet or with the nozzle closer to shore, a number of eddies formed; their number is shown in Figure 6. The eddies photographed in Figure 3 are shown in the run directly below the circled run.

4. QUANTITATIVE MEASUREMENTS

The magnitude of the westward velocity was measured by plotting the trajectories of the centers of the eddies as a function of time. Typical trajectories are shown in Figure 8. Some exhibited uniform speed and clearly were quite well developed with plenty of inertia, others attenuated rapidly from friction. It was desired to compare the westward eddy velocities of many eddies as a function of the formula for velocity of eddies

$$c = \frac{g^*S}{f} \tag{1}$$

which was derived by *Nof* [1983] for an anticyclonic eddy on a sloping bottom with infinitely deep motionless fluid above it. Here $g^* = g \, \Delta \rho/\rho$ is gravity multiplied by the relative density difference between the two fluids (often called reduced gravity), S is the slope of the bottom, and f is the Coriolis parameter. This same formula for velocity was found by *Mory et al.* [1987] using a quasi-geostrophic approximation for a noncirculating eddy with cyclonically circulating fluid above it. We shall discuss the generality of this formalism in section 7.

To calculate the velocity from the formula accurately, it was necessary to determine the density of the salty lens by direct measurements of the salinity of the fluid in the lens. Samples of the bottom dyed fluid were obtained through the use of a syringe and a long tube which was laid on the bottom as the eddy passed over it. When the eddy center passed the tip of the tube, a small sample was drawn

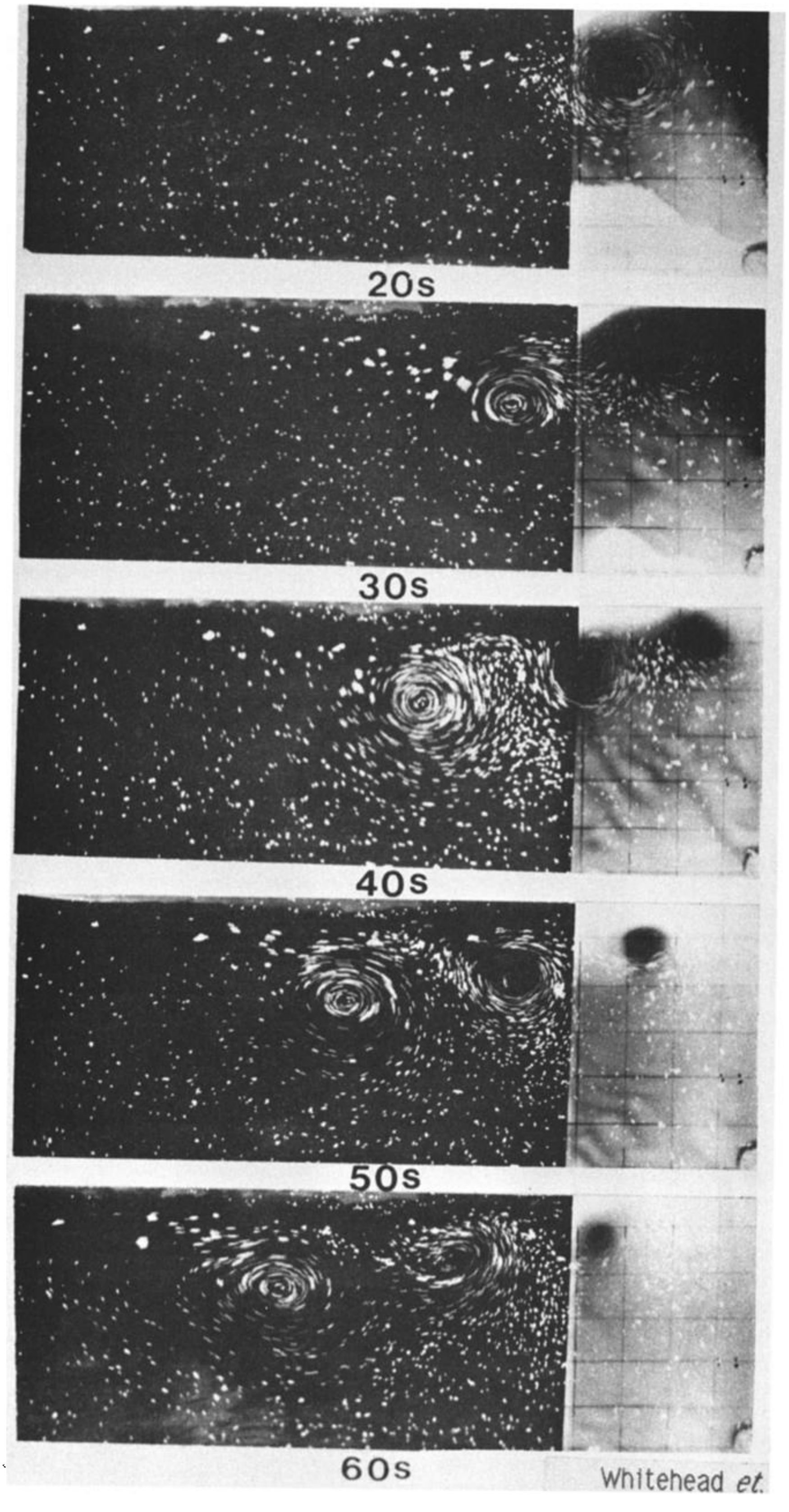

Fig. 4. One-second time exposure streak photographs of surface pellets. The eddies advance over the black background. To the right is a white background that reveals the circular lens of dyed salty water. There is a 10-s interval between frames. The forcing parameters are very similar to those in Figure 3.

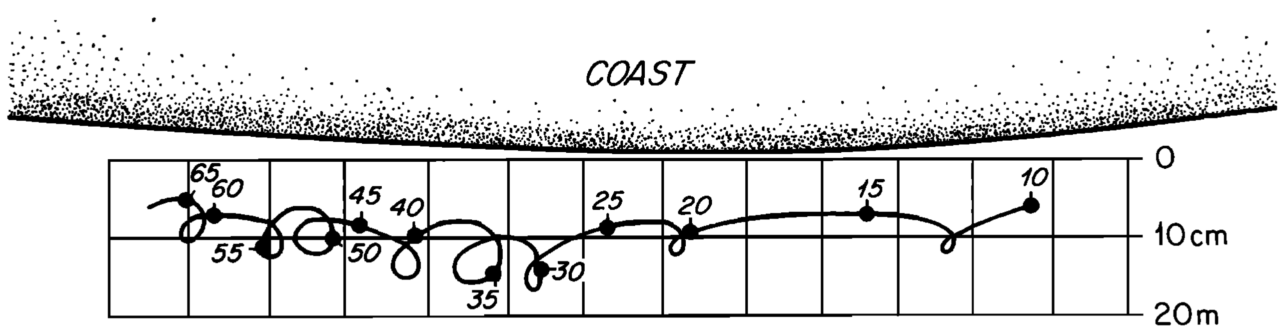

Fig. 5. Trajectory of a surface float trapped over the eddy in the run which is circled in Figure 6. The numbers denote time after an arbitrary starting time.

into the tube and hence into the syringe. The index of refraction of the sampled fluid was measured with an optical refractometer. This method requires a very small volume, and care was taken to insure that the desired fluid was carefully withdrawn without incorporating adjacent fresh water. It was found that the salinity of the sample was considerably less than that of the original intrusive fluid in all cases. Probably the intrusive water was mixed with fresh water by turbulence which was produced either during the initial squirting of the jet or during the gravitational slumping that led to the eddies.

The observed velocities were then plotted against the calculated velocities as shown in Figures 9*a* and 9*b*. Figure 9*a* was from the first experiments in which salinity of the intrusive fluid was approximately $\frac{1}{3}$ of the salinity of the fluid in Figure 9*b*. Figure 9 exhibits large scatter, but the primary reason for this large scatter is that all eddies over the entire parameter space were included in this figure, even those eddies which were weak and poorly formed. Also, scatter naturally arises from the fact that the eddies have continuous stratification. Not only will the density profile probably vary in detail from run to run, but the withdrawal technique only gets a crude measure of the maximum density as well. The mean percentage difference between observed and calculated velocity is 0.80, and although the large scatter is bothersome, it does not seem to be unrealistic in view of the fact that the actual eddies contain numerous features (stratification, friction, finite water depth) not present in two-layer eddies. Thus in the early state the eddy propagation speed is the same order of magnitude as (1). (Included in Figure 7 is one measurement for an eddy formed by fluid injected from above (see section 5).) This is in contrast to Mory et al., who used values of the original density in (1) and did not report agreement between observed speeds and (1).

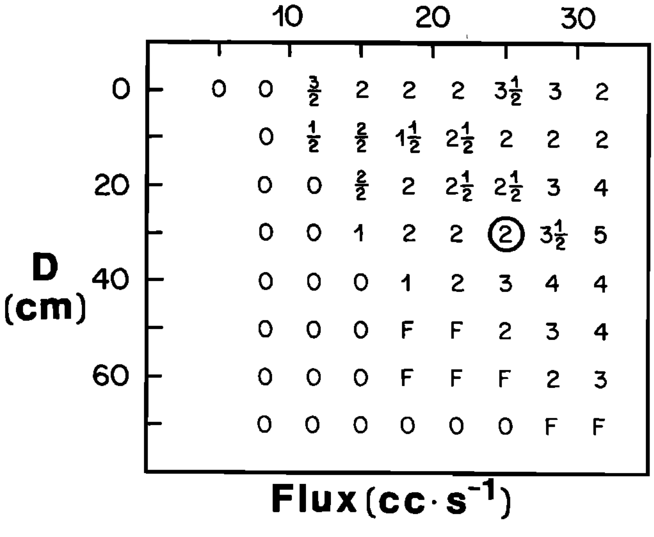

Fig. 6. Regime diagram for experiments in which flux of the jet and the distance of the jet offshore (D) were systematically varied. The numbers denote the numbers of eddies observed. The fractions denote that a number (numerator) of small eddies were formed. F denotes an interesting front in the Ekman layer. The encircled run produced the most distinct eddies. A trajectory from one is shown in Figure 5. The three eddies shown in Figure 3 were from the run directly below the circled run.

The integral constraint discussed below also implies that the fluid circulation velocity in the bottom eddy is relatively small, and we have attempted to verify this by direct observation. Velocity profiles of the bottom eddy were generated by carefully injecting a north-south line of dye along a line 1 to 2 mm off the bottom with a very long tube connected to a syringe. The injected fluid was composed of dyed water with a salinity close to that which was measured in the eddy. Video images were taken of the four runs with the best eddies that were observed. This run has the parameters of the circled run in Figure 6 and corresponds to the photographs in Figure 3. Figure 10 shows the evolution of dye streaks from images 1 s apart. It shows that movement in the bottom eddy is principally translational from east to west, with small additional cyclonic circulations. Thus even the sign of circulation differs from Nof's anticyclonic model. The dye also shows that fluid north of the eddy moves rather uniformly westward. Since the eddy is relatively close to the shore, this flow could be generated by water which cannot be bodily moved offshore to go around the eddy. There is also westward motion of the bottom fluid south of the eddy. It was clearly visible in the video tapes that the westward motion in the bottom fluid was due to the density current which is composed of dense water in the bottom Ekman layer.

Similar dye lines in the top fluid (left column) permit direct measurements of the velocity field of the top eddies. It is clear from inspection that there is strong cyclonic circulation. The areal extent of the counterclockwise circulation of the top fluid is tens of percent larger than that of the lens of dyed dense water and the circulation extends both north and south of the eddy. Further to the south of the eddy there is little or no motion in the water above the bottom.

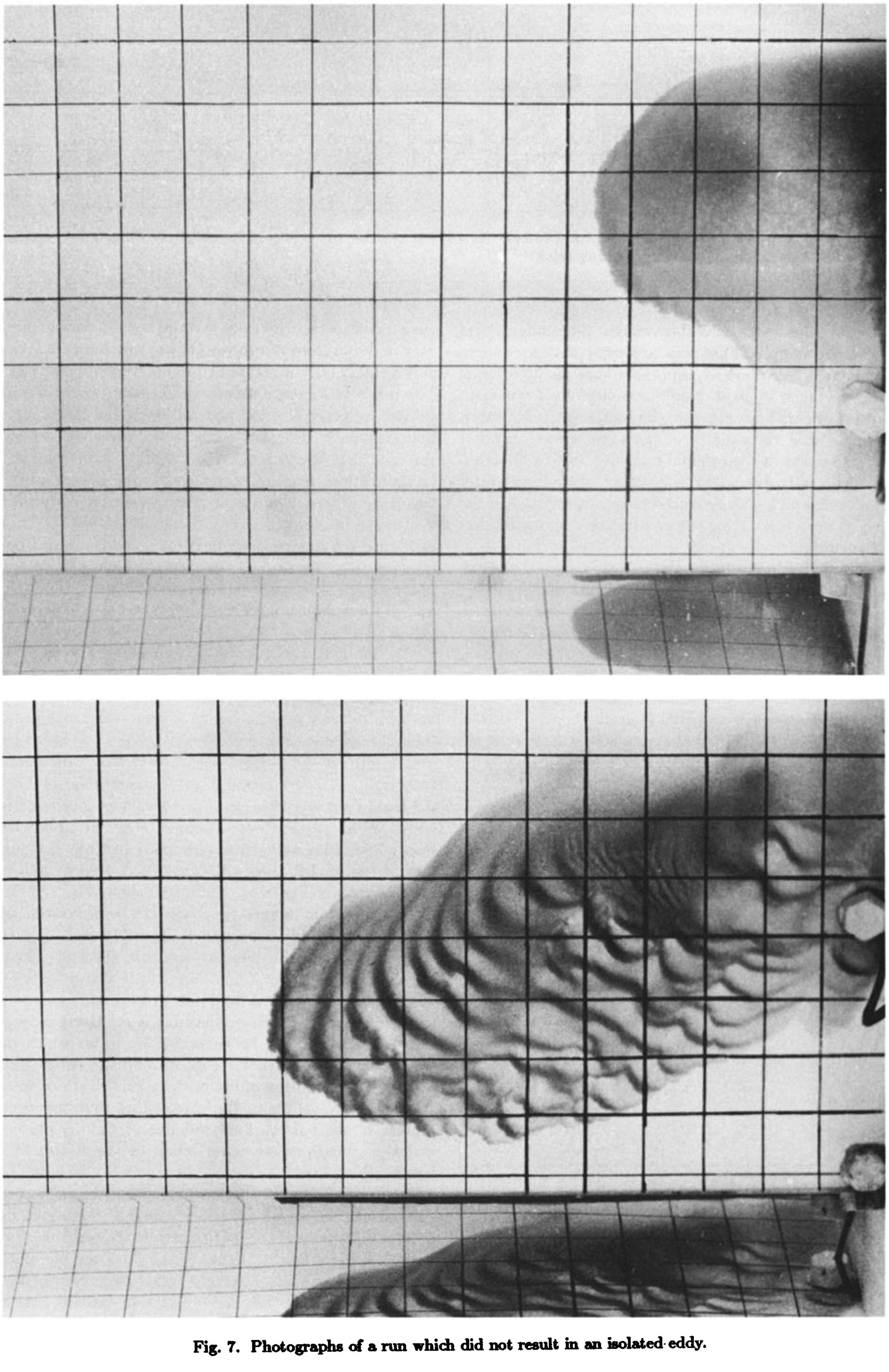

Fig. 7. Photographs of a run which did not result in an isolated eddy.

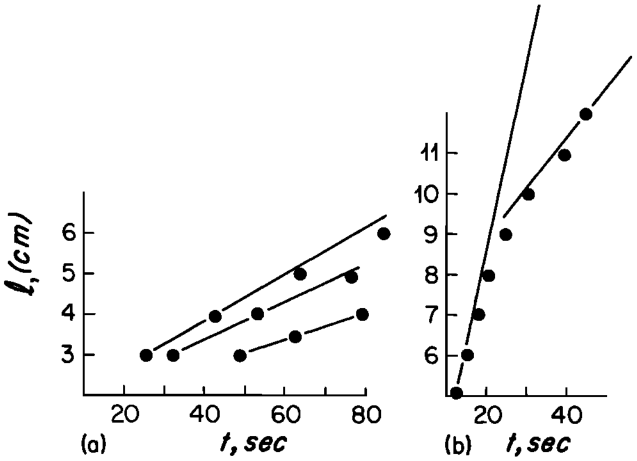

Fig. 8. Typical trajectories of the eddies from which velocity was determined. (*a*) Straight trajectories for which the velocity is easily determined. (*b*) Curved trajectories in which the velocity was markedly decreasing with time. For such cases we used only the initial velocity for Figure 9.

There is also unanticipated westward moving fluid north of the eddy, as there was for the bottom dye line.

In Figure 11 the measured radius of the eddies is presented as a function of a Rossby radius $Ro = \sqrt{g^*H}/f$. Here H is total depth of the fluid at the center of the eddy. Although observed radii are of the same order as the Rossby radius (in fact, roughly 0.8Ro), there is considerable scatter. This arises from a number of factors. First, there is considerable ambiguity about the location of the edge of the eddy. The radius was determined by eye, from the film, and the edge is not distinct. Second, the eddies were not perfectly circular and in those cases, we used half the east-west width for the radius. Third, all eddies were incorporated in this figure and some were small and weak. The ones on the left in Figure 11, in particular, could have been strongly influenced by friction.

5. OTHER EXPERIMENTAL METHODS OF GENERATING THE EDDIES

Four other methods were successful at generating these eddies, which suggests that they are robust structures which

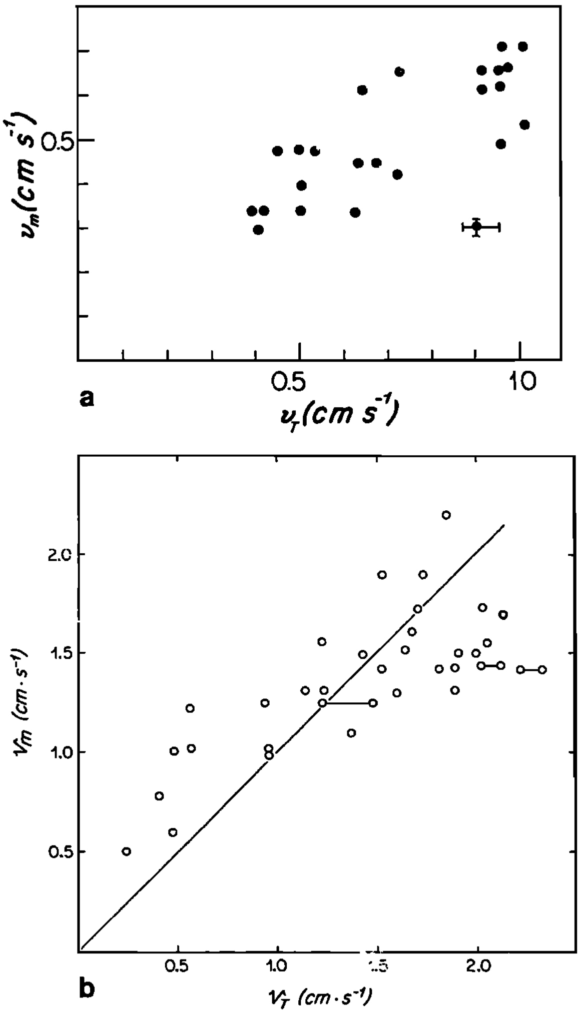

Fig. 9. Measured eddy velocity as a function of predicted velocity v_t. Figures 9*a* and 9*b* denote two experiments with the former having one-third the salinity of the latter. In Figure 9*b*, the circles connected by horizontal lines denote a range of observed velocities.

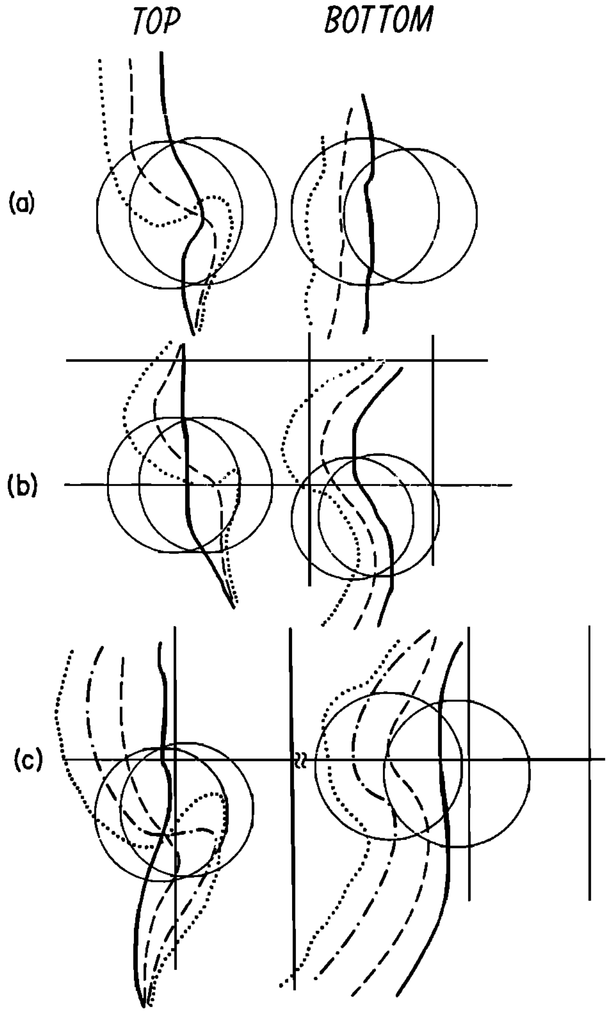

Fig. 10. The evolution on north-south streaks of dye injected (left) just under the top free surface of the water and (right) along the bottom. The outline of the dyed lens of dense water is showed for the first and last streak. The interval between streaks is 1 s.

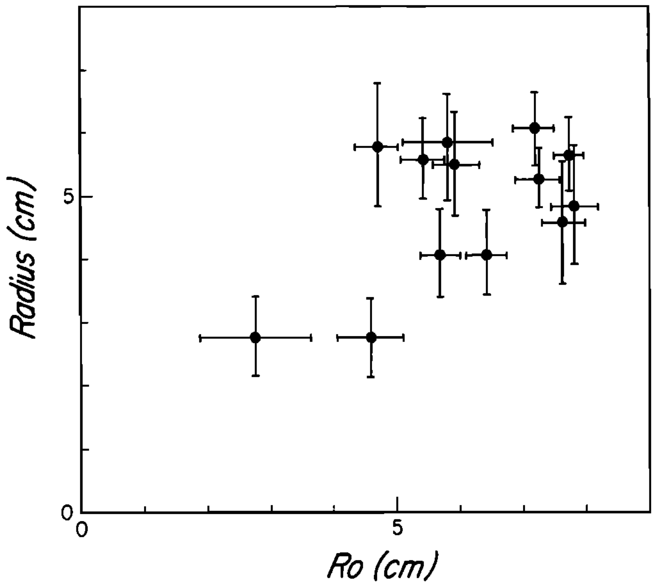

Fig. 11. Radius of the eddies as a function of the Rossby radius of deformation, $Ro = \sqrt{(g^*H)}/f$.

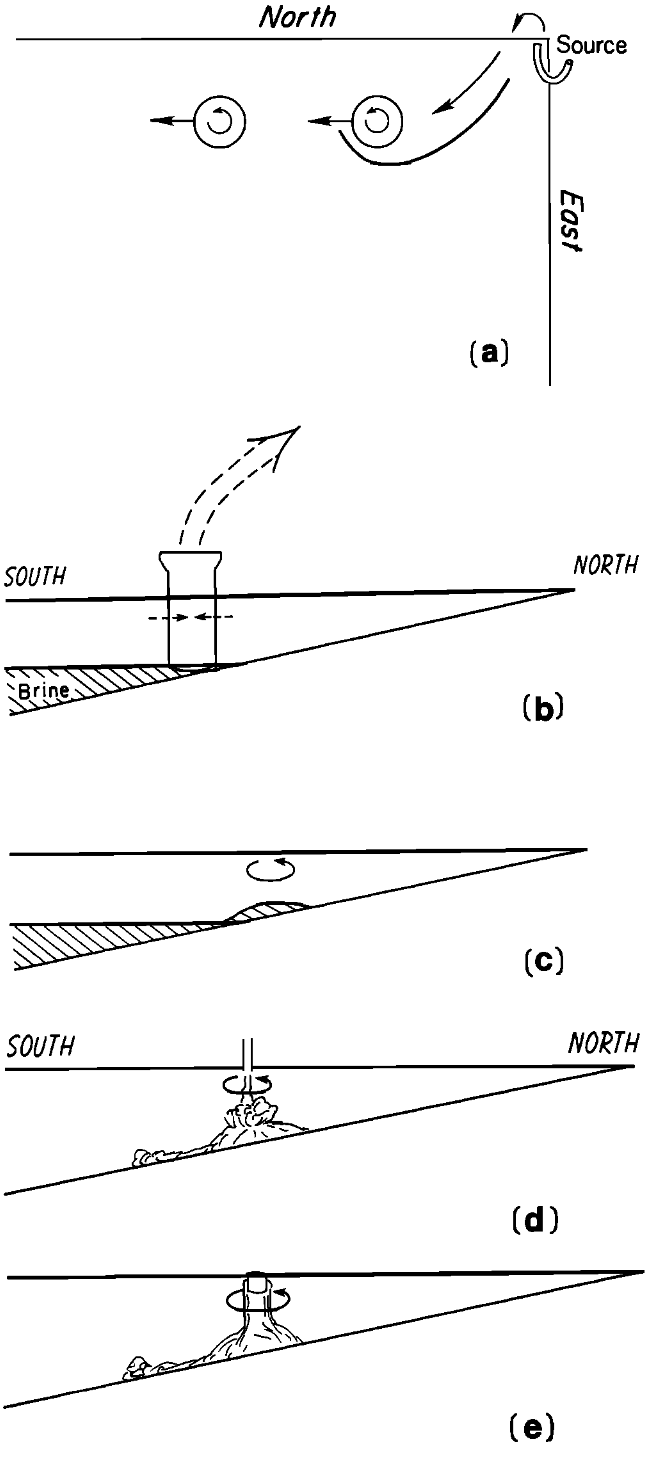

Fig. 12. Sketch of four other methods to generate the baroclinic eddies on a sloping bottom. (*a*) Generation by a density current at a coast. (*b*) Generation by removing a beaker in motionless fluid. This produces a strong cyclonic eddy. (*c*) The cyclogenetic suction over a layer of deep brine lifts up a dome or lens. (*d*) Generation by an inverted turbulent plume. (*e*) Generation by a floating ice cube.

might be anticipated under a variety of conditions. The methods are sketched in Figure 12 with accompanying photographs in Figure 13 and are listed below.

1. A source of dense water at the coast (Figure 12*a*). In agreement with earlier experiments of *Griffiths* [1983], cyclonic eddies were formed with a lens of dense fluid below. There was formation of these coherent eddies only if the density current was turbulent. There was no eddy if the flow was laminar. Instead, the dense water sank down in the bottom Ekman layer, which sometimes exhibited pronounced roll waves, as shown by the 0 data in Figure 6 and photographed in Figure 7. Our distinct impression is that the cyclonic flow in the top fluid is caused by entrainment suction [*Ellison and Turner*, 1969] which pulls fresh water into the density current, and this acts as a sink to the fresh water lying above. This suction then pulls fluid in from greater radii and generates cyclonic flow. This suggested mechanism differs from the inertial wave radiation–cyclogenesis mechanism suggested by *Griffiths* [1983] which should have been visible over roll waves. The experiments described below also support the above mechanism and do not seem to be consistent with cyclogenesis by internal wave radiation.

2. Removal of a known volume from the water over a reservoir of salt water (Figure 12*b*,12*c* and 13*c*,13*d*). This produces a cyclonic eddy which lifts a lens of bottom fluid and forms our eddy of interest. In our experiments we generated suction by removing water with a syringe or by removing a beaker from still water. The completed eddy then propagated westward from the generation zone. There was a clear tendency for the generated eddy to drift north as well as west (a feature observed by *Mory et al.* [1987]).

3. A plume of dense water sinking from the top surface. This makes large and energetic eddies. We believe that cyclogenesis arises from entrainment of fresh water by the turbulent plume as it sinks. The turbulence mixes the fresh water with the salty water and forms the final water which resides in the bottom lens. We tested the Stern integral relation [*Mory*, 1983] for two isolated eddies generated in this way (see next section). We also found that both the observed predicted drift speed of one of the eddies was 0.12 cm/s (see section 4). When the salt water was continued for 10 or 15 mins, a street of eddies would slowly accumulate to the west as newly formed eddies grew, propagated westward, and vacated the generation region (Fig-

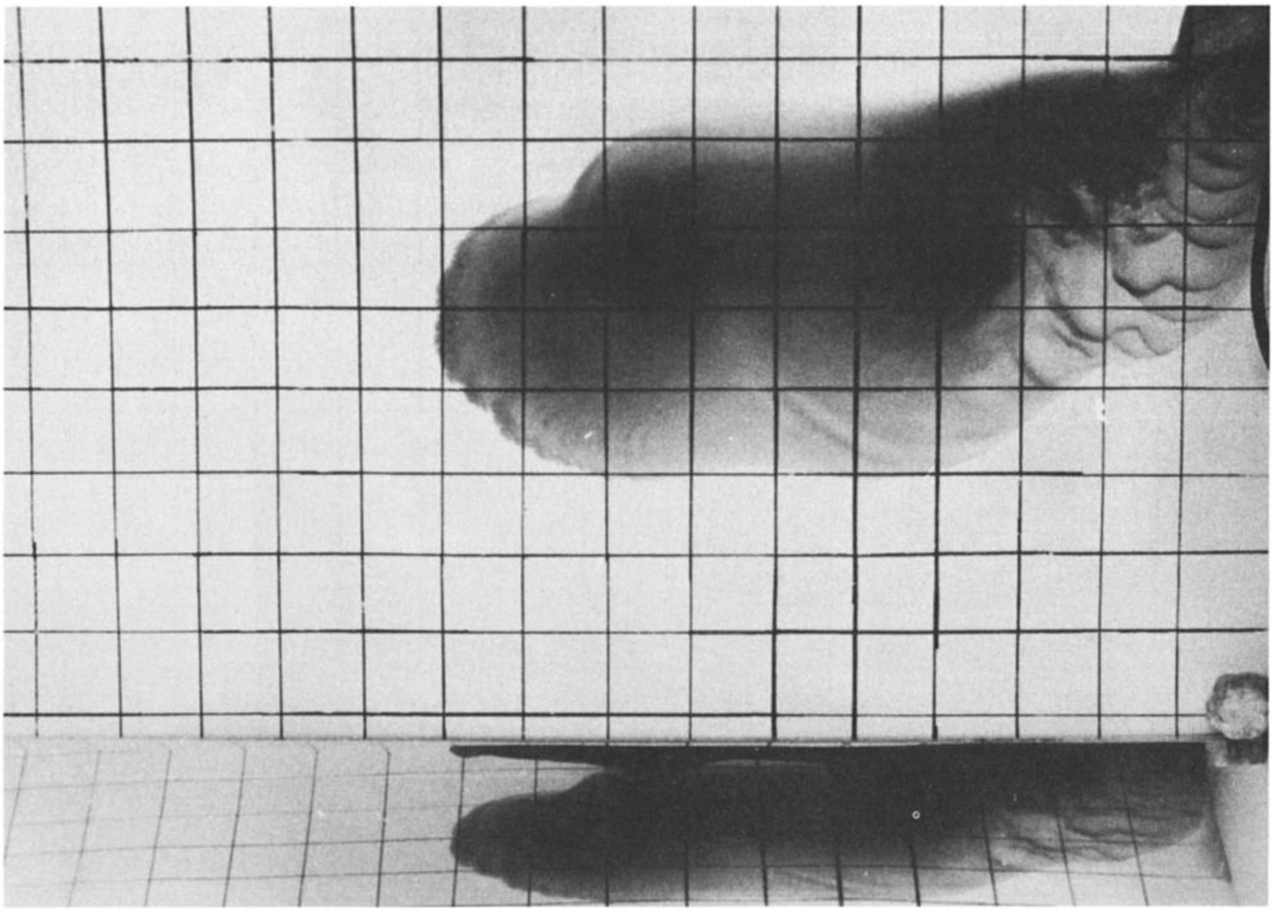

Fig. 13a

Fig. 13. Photographs of eddies generated by the four mechanisms shown in Figure 12. (*a*) A source at a coast makes a density current which flows offshore and bends to the west. Two eddies are forming. (*b*) Forty seconds later, the fluid in the Ekman layer has continued to the deep end of the tank and two large eddies remain. They continued to move westward. (*c*) A beaker is removed over a reservoir of brine. (*d*) One eddy has formed and moved up the slope and to the west. (*e*) A turbulent plume of dyed salty water over deep water produces cyclonic flow above a dome of brine. (*f*) Sixty seconds later a train of eddies extends west of the source. (*g*) One hundred twenty seconds later the train has become irregular. (*h*) A floating ice cube generates an eddy in a manner similar to the plume, except the ice cube remains trapped in the surface eddy and propagates westward with the eddy.

ures 12*d* and 13*e* through 13*g*). A movie of this is available for viewing.

4. A variation of method 3 is to place an ice cube in the water over a sloping bottom. We believe that cyclogenesis arises from conduction of the low ice temperatures to the surrounding water, which then sinks and forms a cold dense lens. We placed pellets on the surface and clearly saw them drawn radially inward toward the ice cube. Also, dye in the ice sank and was diluted as it sank. Since the ice cube drifts with the eddy, a street does not form, but the eddy continues to strengthen indefinitely.

We also placed a nozzle in the center of the sloping bottom and successively pointed it sideways in all four directions. Parameters were set to the value which led to optimal eddies before, and at least one eddy was formed in all four cases.

6. TEST OF THE CIRCULATION-PRESSURE INTEGRAL

We have used photographs of plume-generated eddies to test the integral theorem of Stern [*Mory*, 1983] which is reviewed in section 7 (equation (26)). In cylindrical coordinates this can be written

$$\int_0^{2\pi} \int_0^{r_1} (p_1 + g^* h)\, r\,dr\,d\theta = 0 \tag{2}$$

where p_1 is pressure of the overhead fluid divided by its density, g^* is reduced gravity for the lens of heavy fluid, and h is the vertical thickness of the lens. For a sufficiently isolated eddy, we may choose for r_1 any radius larger than the eddy radius.

The pressure p_1 is determined by the velocity field in the top layer. Assuming an axisymmetric, inviscid, time independent eddy, we have the cyclostrophic relation,

$$fv + \frac{v^2}{r} = \frac{dp}{dr} \tag{3}$$

The eddies generated in the lab have $O(1)$ Rossby numbers so that the centrifugal force term can not be ignored. Velocity fields were determined by streak photographs of small (1 mm × 3 mm), white, rectangular pellets strewn on the surface over the eddy.

The other term is determined by noting that the darkness

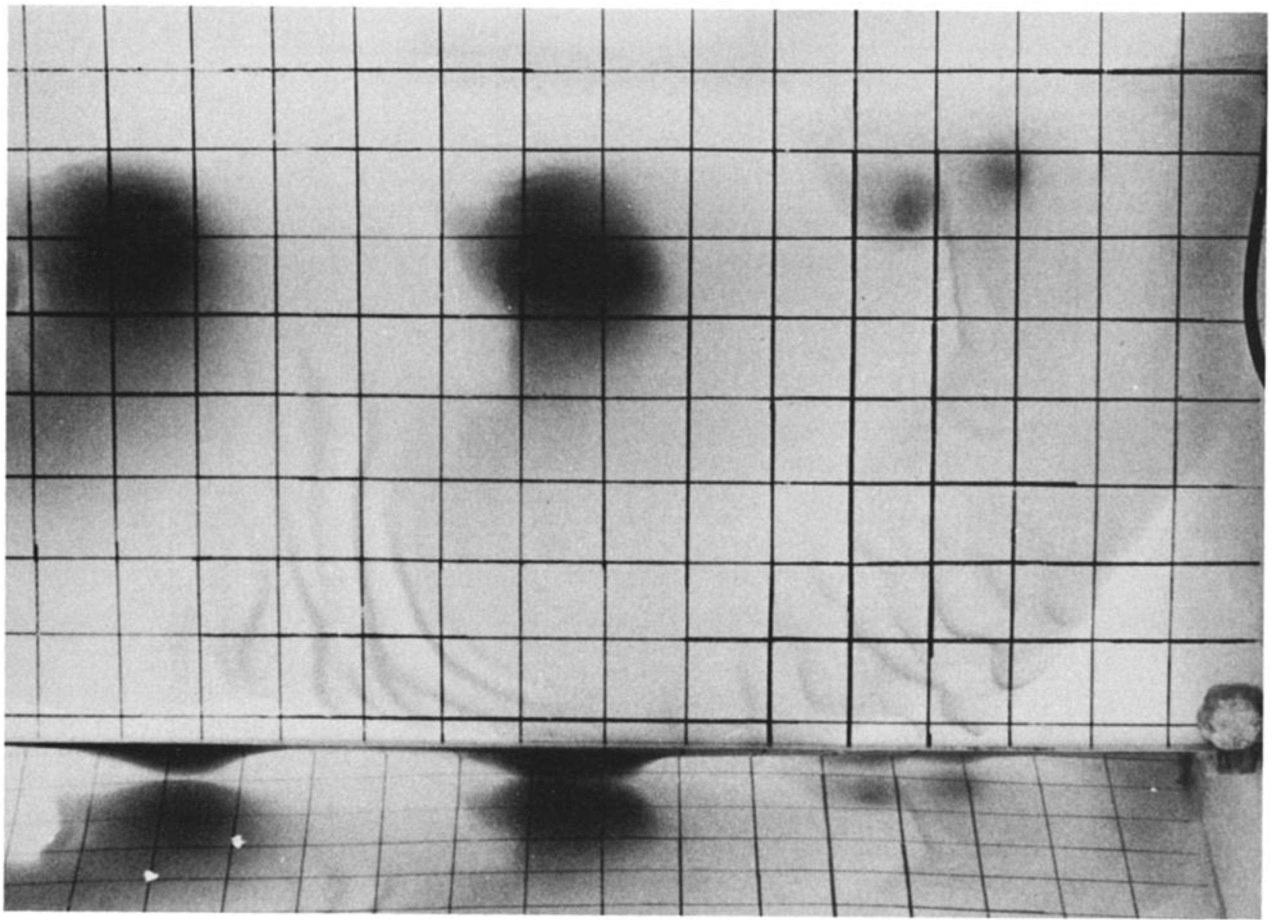

Fig. 13b

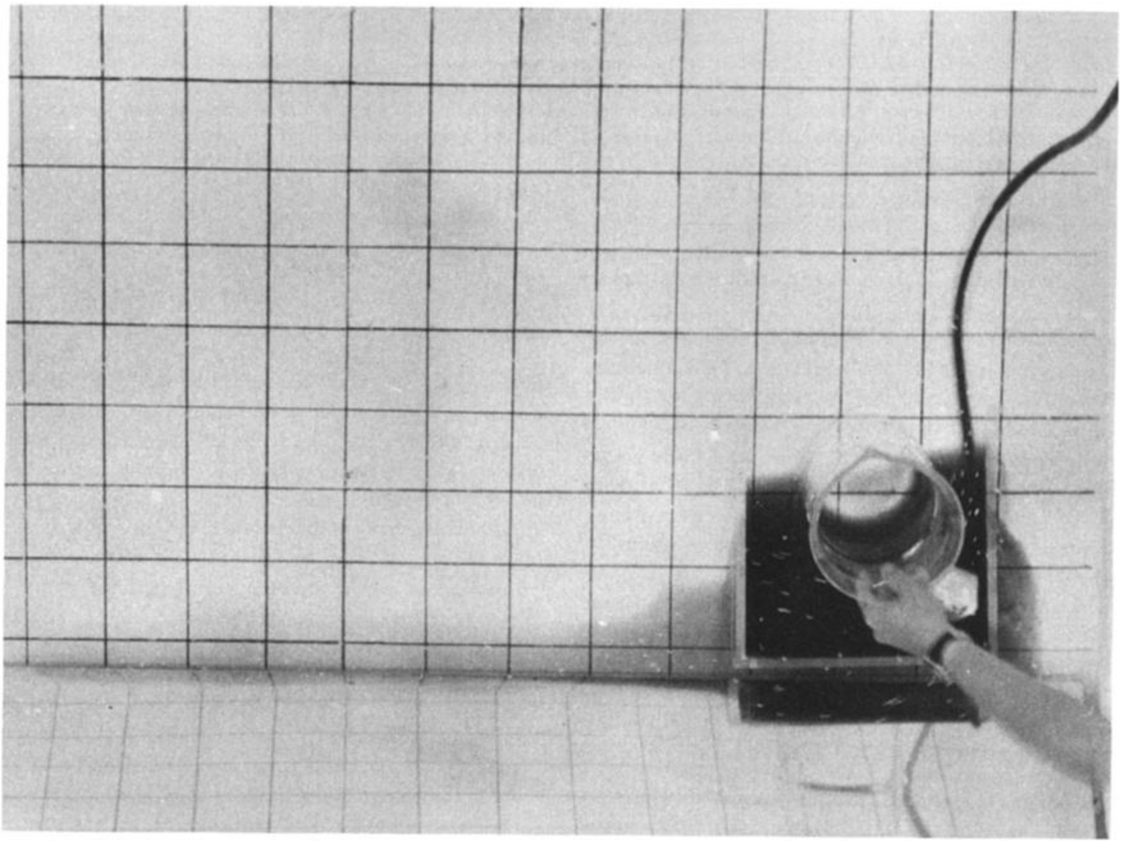

Fig. 13c

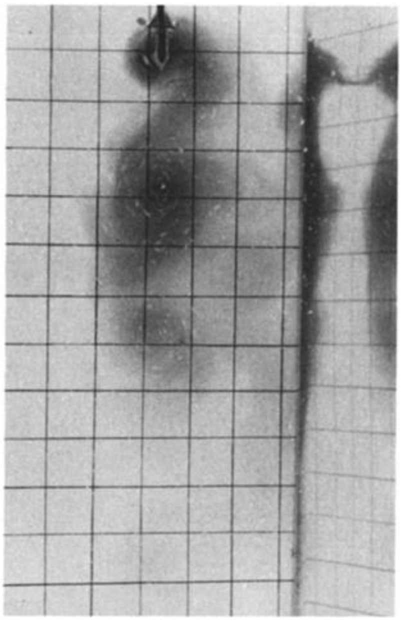

Fig. 13e

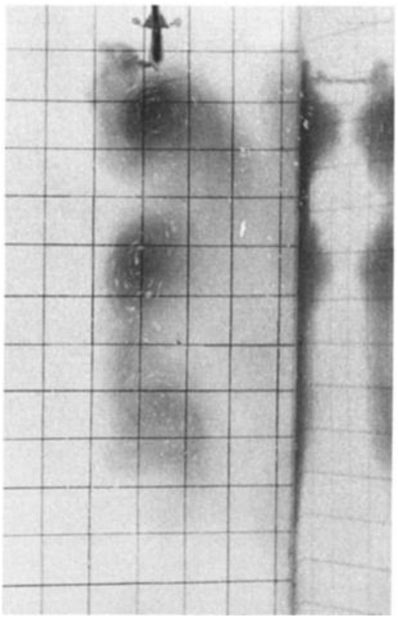

Fig. 13f

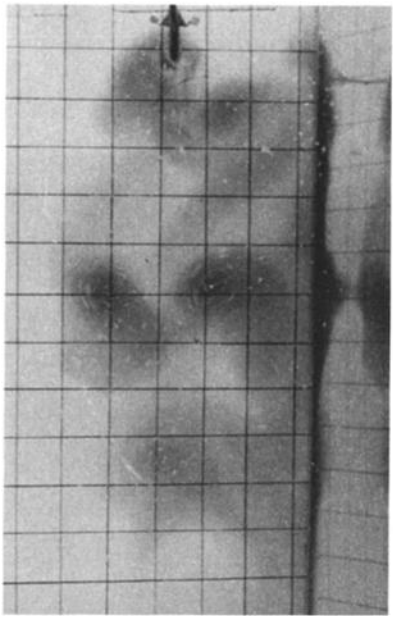

Fig. 13g

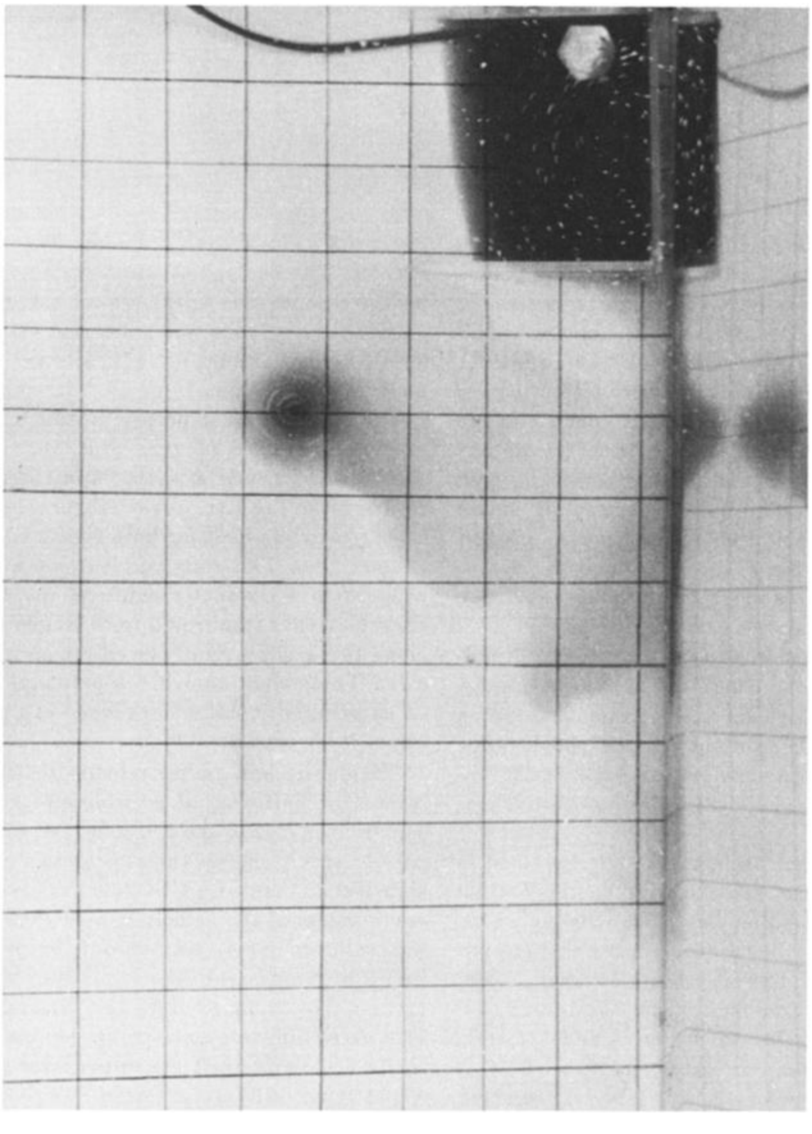

Fig. 13d

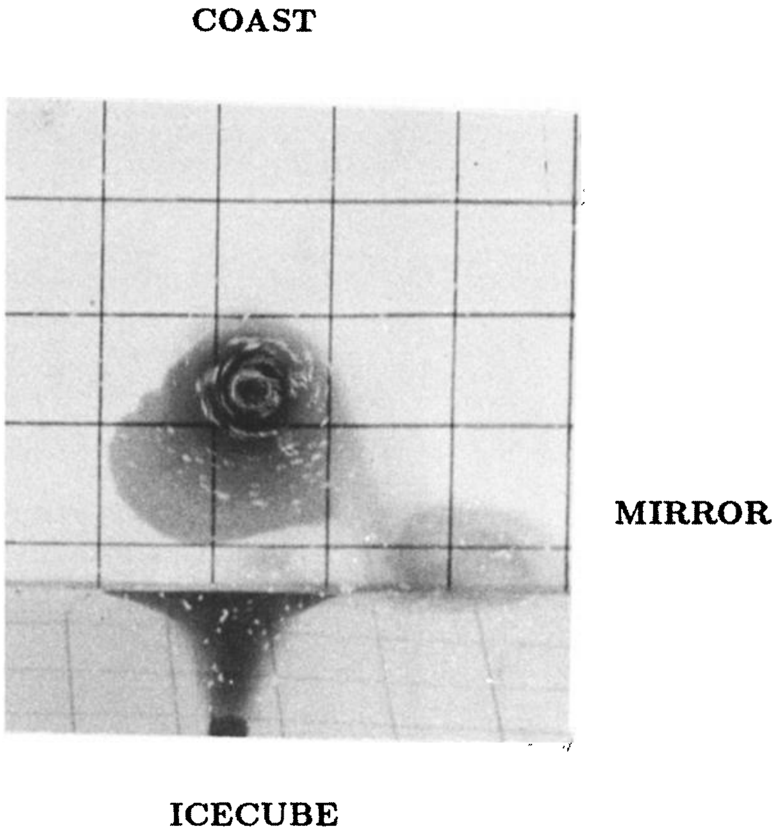

Fig. 13h

of the dyed salty water in the lens, when viewed from above, is proportional to g^*h. "Darkness" is measured by transferring the photo via video camera to a computer-accessible digitized image array with 512 pixels in the horizontal and 480 in the vertical. Each pixel is represented by an integer from 0 to 255 proportional to light intensity. This integer is converted to g^*h by a calibration curve from an image of a wedge-shaped enclosed reservoir of water of known dye concentration. The reservoir sits on the bottom of the tank and has the same 1:5 slope as the tank bottom. This makes for a linear relation between concentration times depth and measured light intensity. Since the relation between dye concentration and density is known, this gives a measure of g^*h.

A white bottom was used in the rotating tank. Ambient water was dyed with about 0.07 ml/l saturated potassium permanganate solution. This concentration was strong enough to make white pellets on the surface visible while weak enough to allow measurement of the darker salty water, which was dyed with 10 ml/l saturated potassium permanganate solution.

The eddies were generated using method 3 described in section 5: a plume of dense water sinking to the bottom from the top surface. (An earlier study was conducted using the same measurement techniques described here but with eddies generated by a coastal jet as described in section 2. These eddies appeared to confirm the integral relation but the eddies were close to the shore and not truly isolated from the coast.) Each test eddy had $f = 0.83\ \mathrm{s}^{-1}$, $S = 0.2$, fluid depth at source $H = 13.3$ cm, injected $g^* = 33.3\ \mathrm{cm/s}^2$, and a volume flux of $3.57\ \mathrm{cm}^3/\mathrm{s} \pm 10\%$ for 45 s. The lens radius was 5 cm for the first run and 6 cm for the second, lens thickness was 4.4 cm for both runs, and g^* for the two runs was $2.3\ \mathrm{cm/s}^2$ and $4.1\ \mathrm{cm/s}^2$, respectively. This measure of g^* is based on depth-integrated g^* computed below.

Two runs were conducted. In run 1, the dye distribution was photographed (Figure 14a), then pellets were strewn on the surface, and a photograph of the streaks was taken 15.5 s after the dye photo (Figure 14b). For run 2, the same photo was used for both streak and dye measurements (Figure 14c). This eddy was less well-formed than the run 1 eddy, with a distinctly elliptical (as opposed to circular) shape. Streaks from run 2 were binned into two groups, one along the major axis of the ellipse and one along the minor axis. These were analyzed separately, as if each was from an axisymmetric eddy, in order to estimate the value of the upper layer pressure.

Tangential and radial velocity distributions were determined by digitizing all possible streaks. The velocity as a function of radius are given for the raw velocities in (Figures 15 to 17) and for the same data smoothed with a Gaussian filter (Figures 18 to 20) . The smoothed azimuthal components of the velocities were then multiplied by $\pi r \Delta r$ and summed for an estimate of the pressure integral. The flat, low-speed part of the azimuthal velocity distribution at large r was excluded from the integral on the assumption that these non-zero data points represented noise in the velocity field. For run 1 the upper layer pressure integral was found to be $-613\ \mathrm{cm}^4/\mathrm{s}^2$ when velocity was integrated from

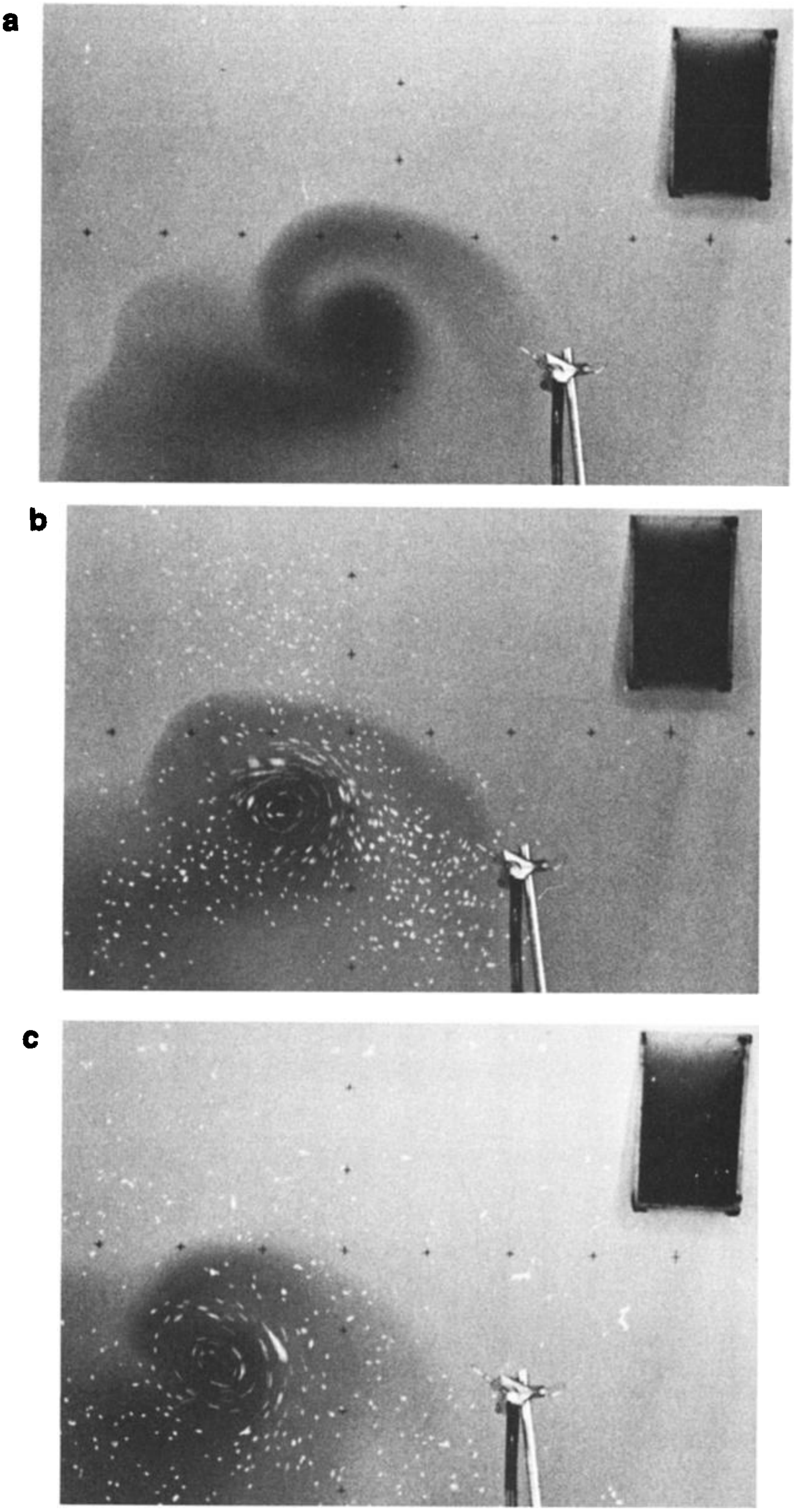

Fig. 14. Photographs of two plume-generated eddies used to test the integral relation: (*a*,*b*) first eddy and (*c*) second eddy.

$r = 0$ to $r = 10.74$ cm. For run 2, the corresponding numbers were -576 cm^4/s^2 integrating to $r = 11.34$ (minor axis) and -820 cm^4/s^2 integrating to $r = 10.91$ (major axis).

The dyed ambient water contributes a significant nonuniform background darkness to the digitized grey-scale image. In order to cancel this background, a "background" image, which shows the tank before the salty dyed water is introduced, is subtracted from each eddy image. Contours (in arbitrary machine units) of each eddy after subtraction are

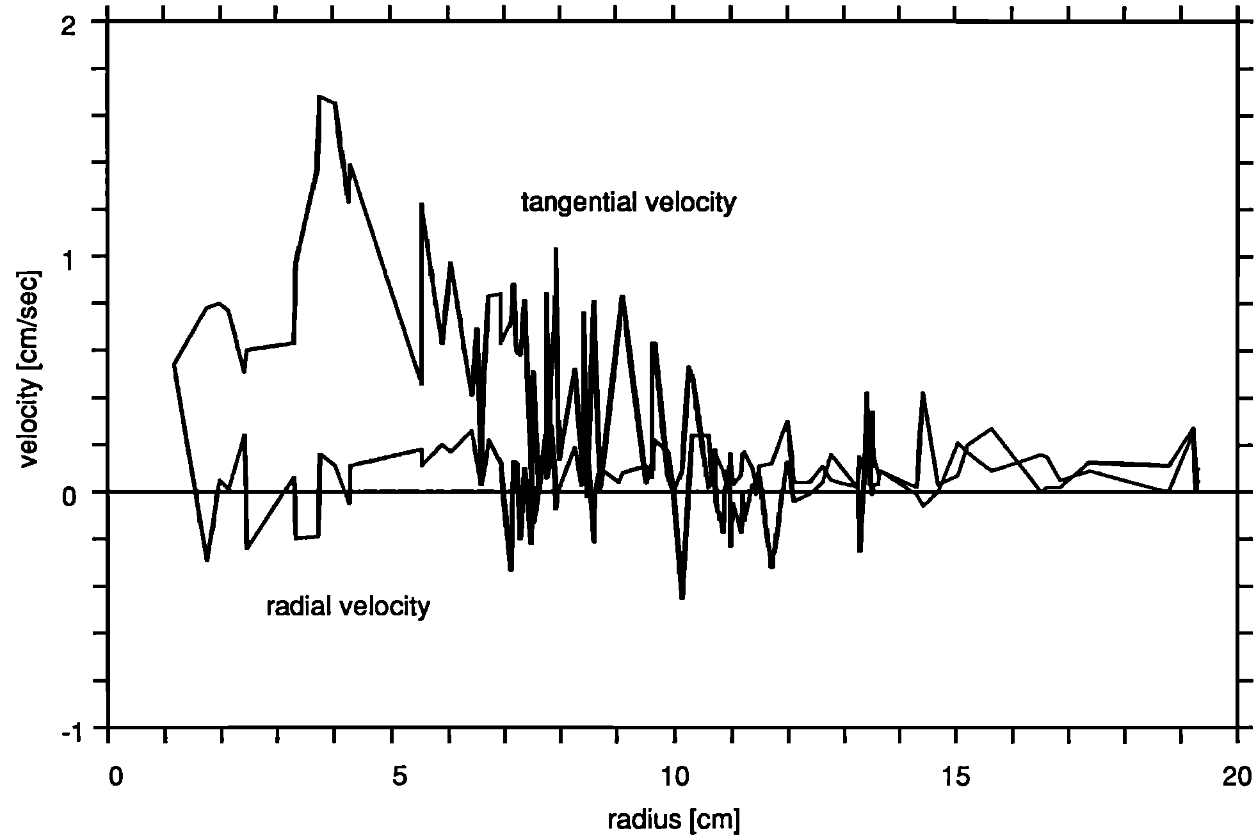

Fig. 15. Tangential and radial velocities of the fluid above the first eddy. These were used to test the integral relation.

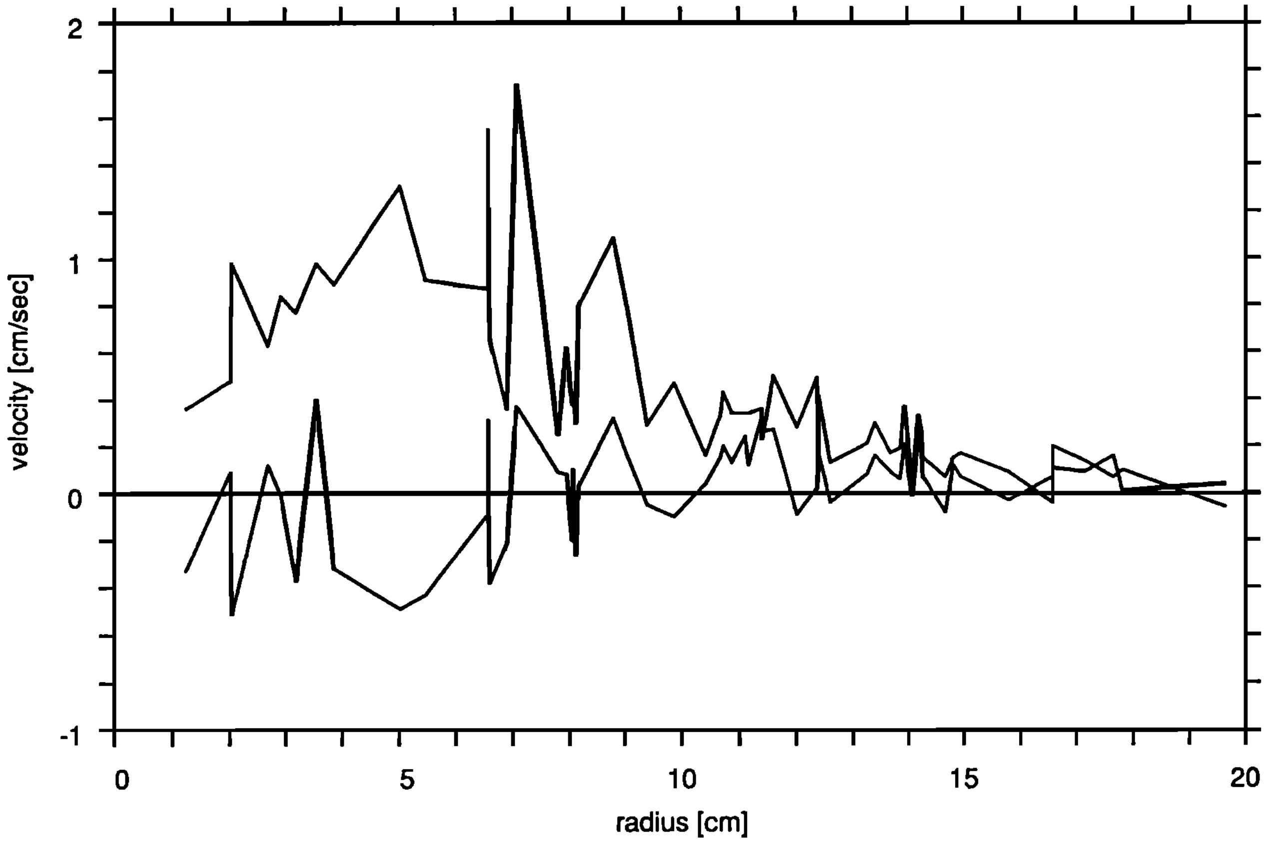

Fig. 16. Tangential and radial velocities in the major axis of the fluid above the second plume-generated eddy.

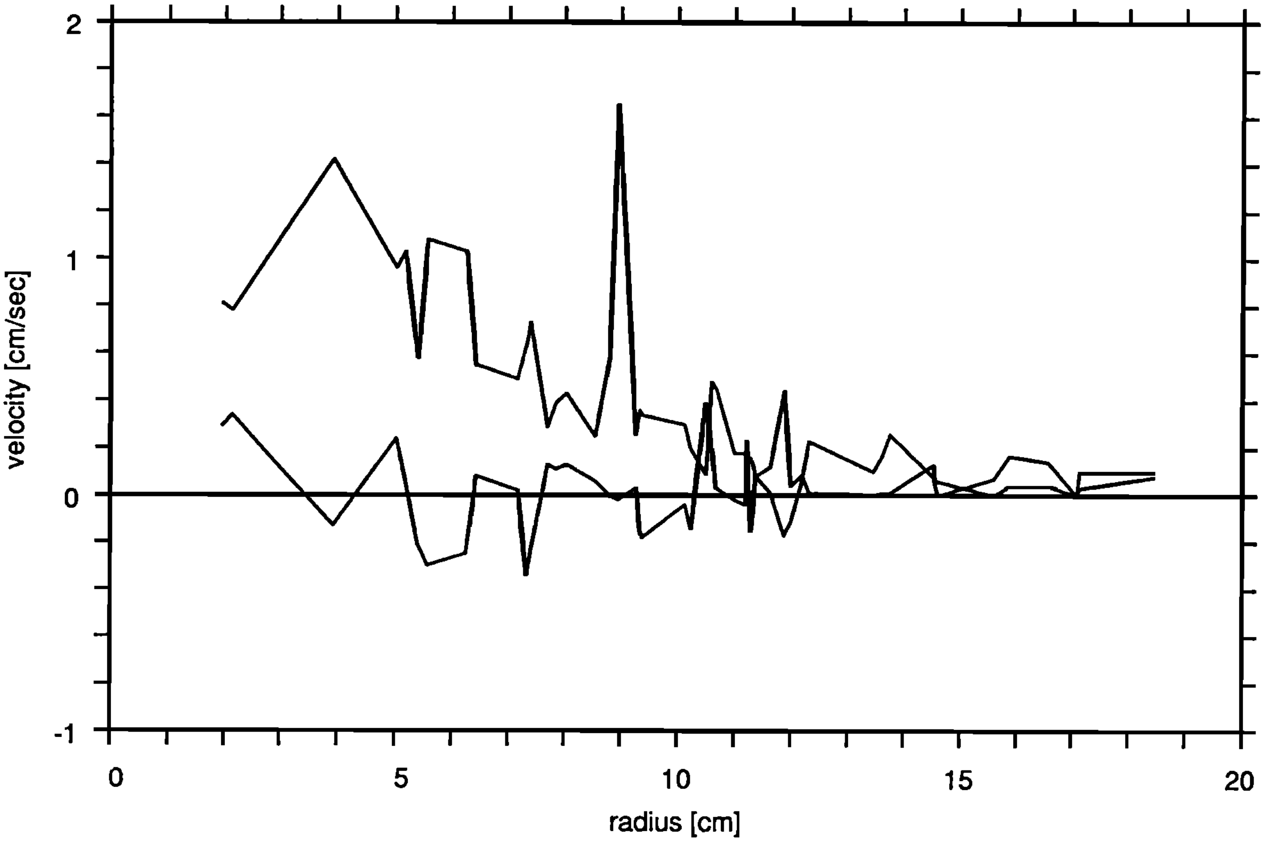

Fig. 17. Tangential and radial velocities in the minor axis above the second plume-generated eddy.

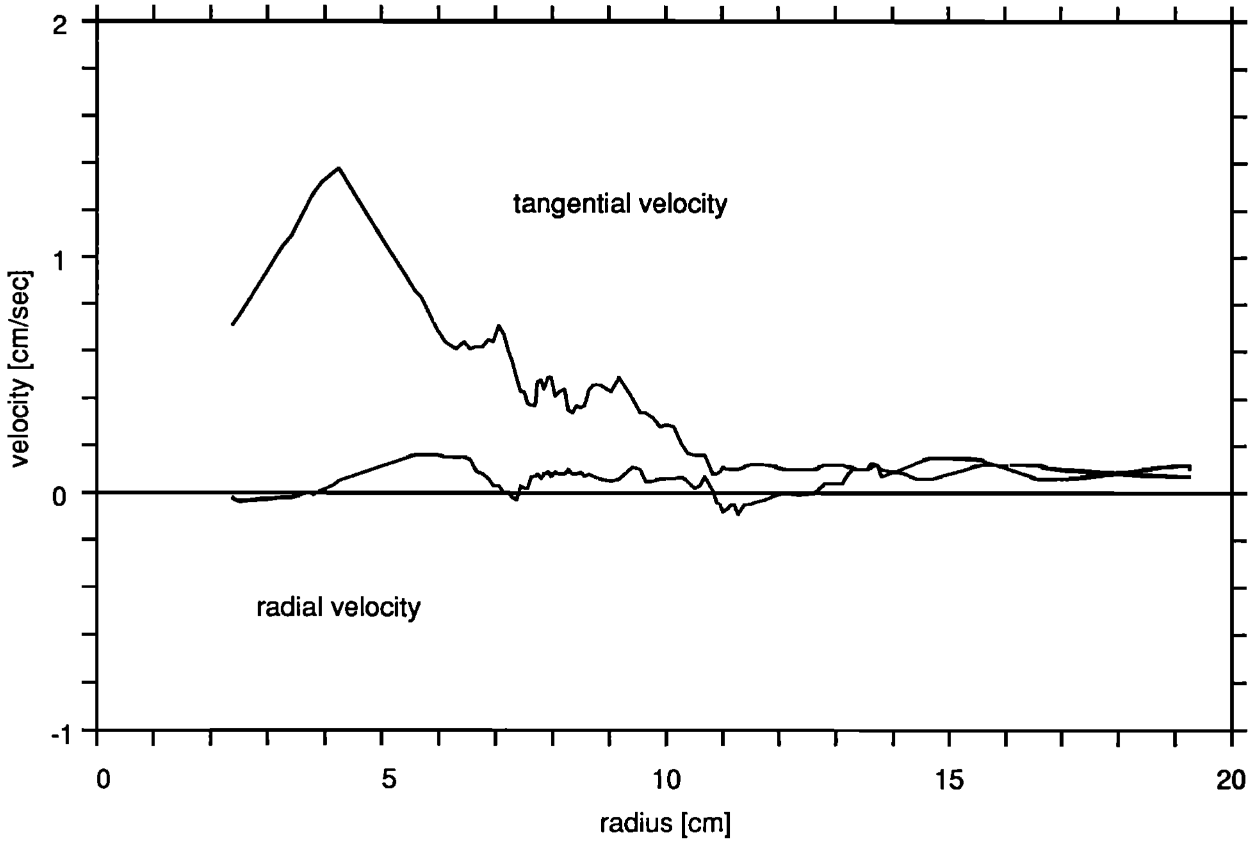

Fig. 18. Smoothed azimuthal velocities for the first plume-generated eddy.

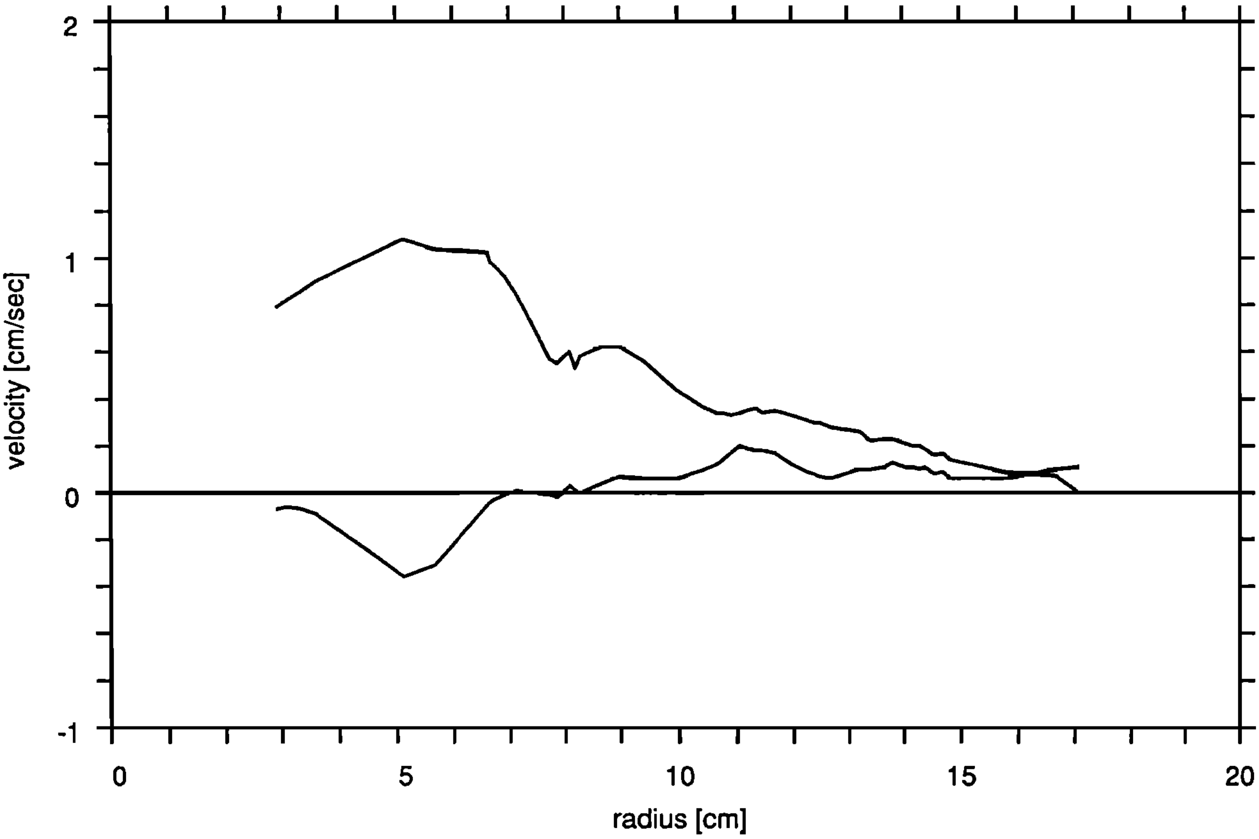

Fig. 19. Smoothed azimuthal velocities for the major axis of the second eddy.

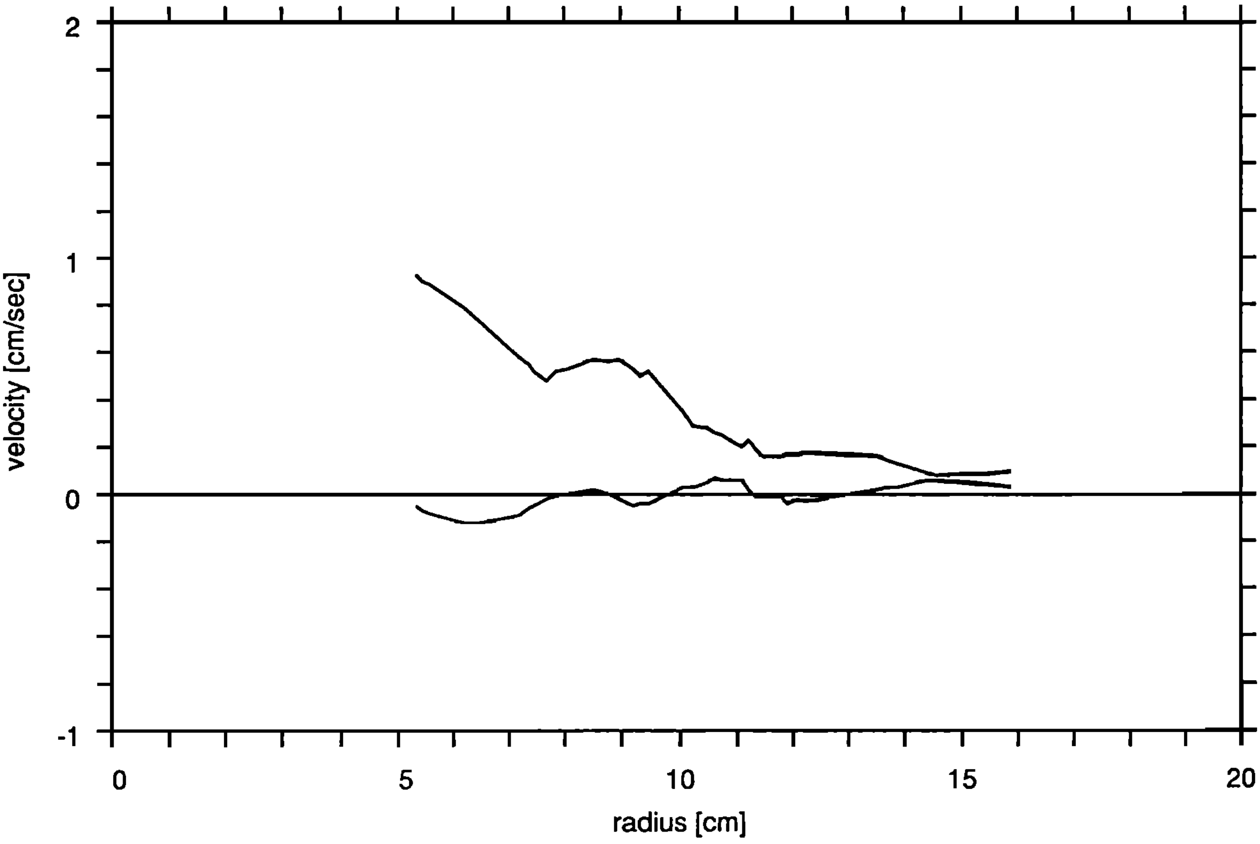

Fig. 20. Smoothed azimuthal velocities for the minor axis of the second eddy.

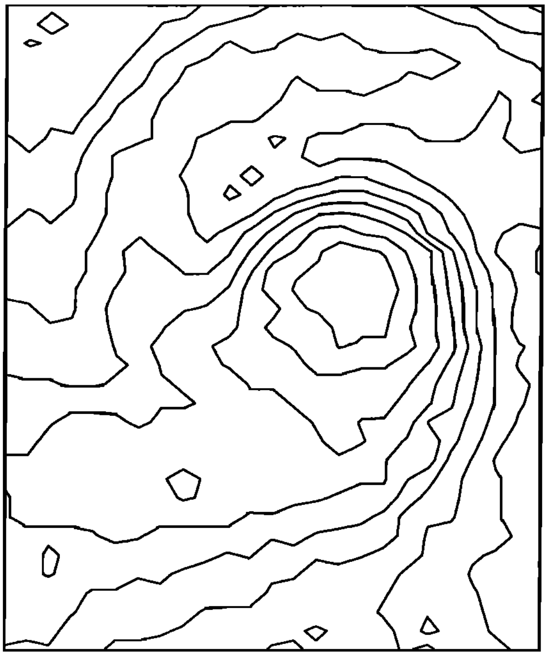

Fig. 21. Greyness contours for the first eddy in arbitrary machine units.

displayed in Figures 21 and 22. For run 2, pixel values for the larger streaks were replaced with the intensities of neighboring pixels. These streaks would probably have changed the darkness measurement by at most a few percent.

To transform the greyness in machine units to a measurement of g^*h, a wedge-shaped reservoir contained the same amount of dye as the injected fluid and had a thickness that varied linearly from zero to approximately 3 cm. The background greyness to be subtracted from each reservoir is taken from the same image just to the "west" of the reservoir. The "north-south" reservoir profile (in machine units) is shown in Figure 23. The profile of the same reservoir in run 2 is nearly identical.

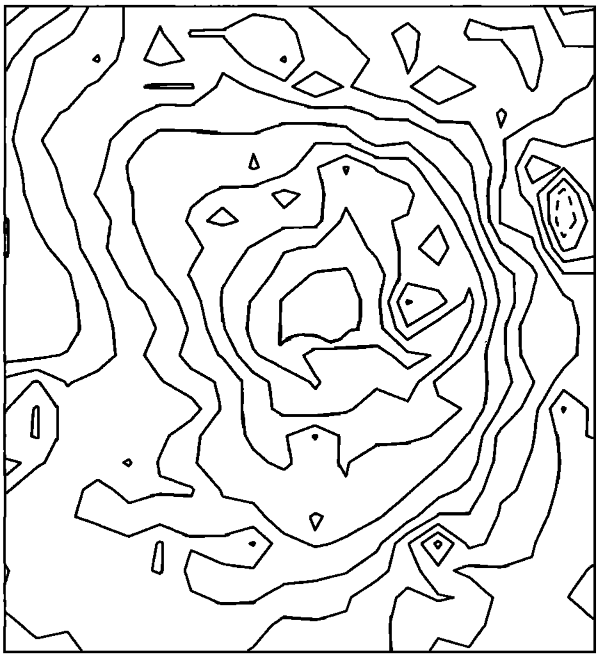

Fig. 22. Greyness contours for the second eddy.

Since the integral relation was derived for the inviscid case, we exclude from our measurement the dark salty bottom Ekman layer, which extends over a larger area than the eddy itself. We can not directly measure the thickness of this layer underneath the eddy, but we assume that it is the same thickness as the part of the layer immediately surrounding the eddy. There is also no clear demarcation between the eddy proper and the surrounding Ekman layer. For measurement of the buoyancy part of the integral we define the eddy to be contained by the largest approximately axisymmetric darkness contour (run 1) or the largest approximately elliptical contour (run 2). The buoyancy integral computed with the best contour for run 1 (pixel values not less than 35 in Figure 21) is 426 cm^4/s^2. For run 2, for minimum pixel of 34 the integral is 704 cm^4/s^2, and for minimum pixel of 35 the integral is 627 cm^4/s^2.

Thus for run 1 the upper layer pressure integral of 613 $\text{cm}^4\ \text{s}^{-2}$ was about 50% greater than the buoyancy integral of 426 $\text{cm}^4\ \text{s}^{-2}$. For run 2, the two pressure integral estimates of 576 and 820 $\text{cm}^4\ \text{s}^{-2}$ encompassed the two buoyancy integral measurements, with a spread of about ± 15% from the average to the extreme measurements.

Several factors limit this measurement to little better than a factor of 2 agreement. Most important is the uncertainty in separating the Ekman layer region from the eddy proper. Reasonable different choices for the bounding contour of the eddy region yield up to 40% differences in the integral measurement. The pressure measurement is also extremely sensitive to the velocity field at large radii. For instance, including the low-velocity data points at large r would nearly double the top layer pressure integral.

Figures 24 and 25 compare upper layer pressure and g^*h as functions of radius for the two eddies. Pressure is integrated from the tangential velocity distribution, while g^*h is calculated from azimuthal averages of the digitized eddy images. These diagrams show us that the buoyancy is more intense and concentrated at smaller radii than the pressure anomaly in the upper layer. The maximum g^*h of the eddies yield an internal deformation radius of 4.0 cm for run 1 and 5.2 cm for run 2. The actual lens radii measured from Figures 24 and 25 are 5 cm and 6 cm.

7. THEORETICAL CONSTRAINTS AND NUMERICAL SOLUTIONS

The experimental results demonstrate the need for a more focused theory as present solutions cannot be simply altered to incorporate all the complexities of the laboratory. Instead, it is necessary to reformulate the problem from general governing equations. Thus here we establish results on the nature of two-layer eddies over a slope which can be tested against laboratory experiments. The dynamic equations for the system, under the hydrostatic Boussinesq approximations, are

$$\underset{\sim}{u}_{1t} + \underset{\sim}{u}_1 \cdot \nabla\, \underset{\sim}{u}_1 + f\,\hat{k} \times \underset{\sim}{u}_1 = -\nabla p_1 \tag{4}$$

$$-\,h_t + \nabla_1 \cdot \underset{\sim}{u}_1\,(H - h - Sy) = 0 \tag{5}$$

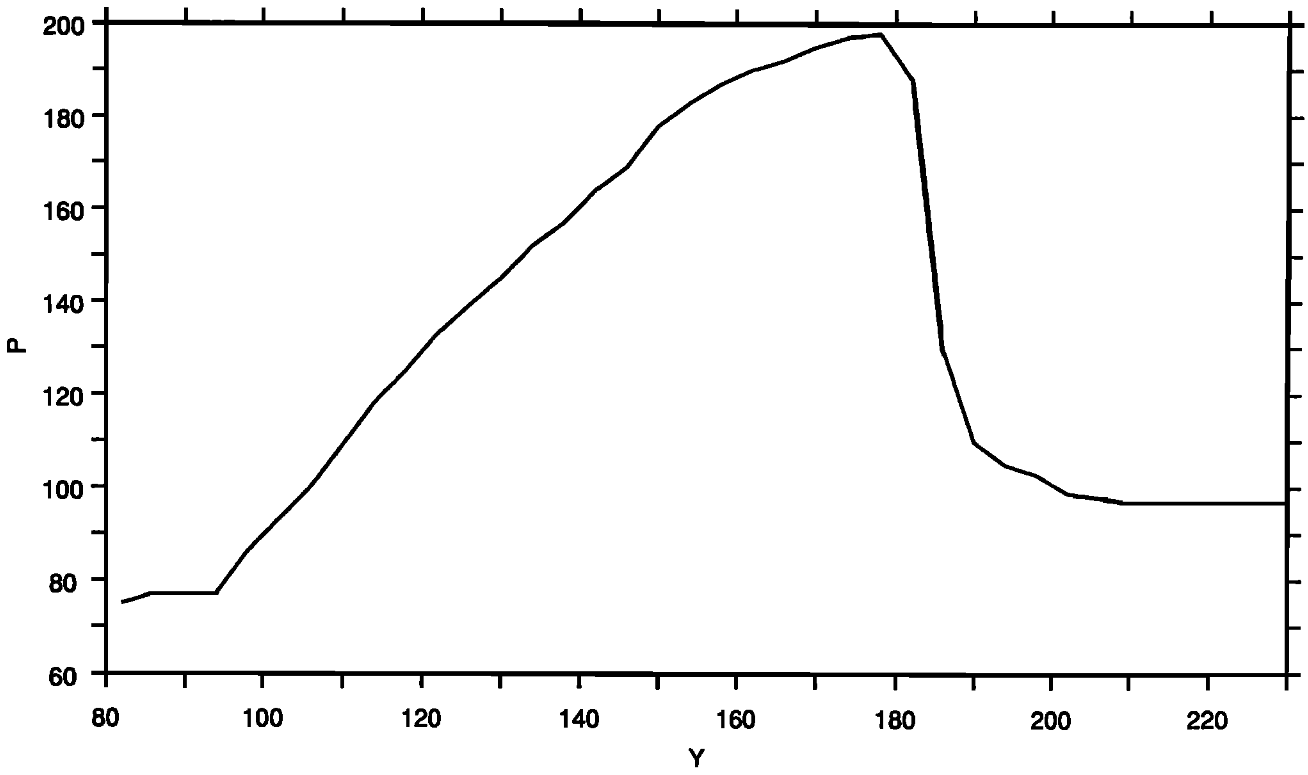

Fig. 23. Greyness profile of reservoir for run 1. Each data point represents the average of a 16-pixel square.

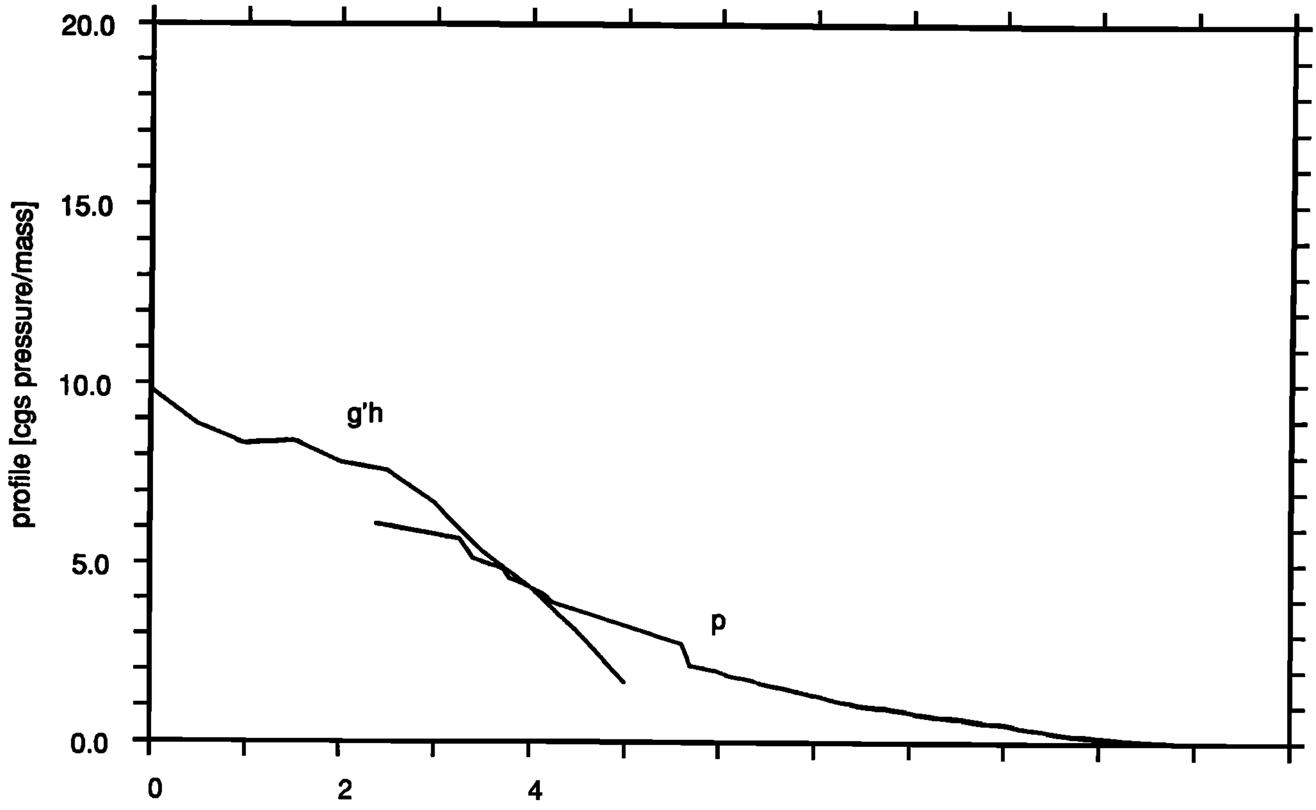

Fig. 24. Plot of p_1 and g^*h as functions of r for the first plume-generated eddy.

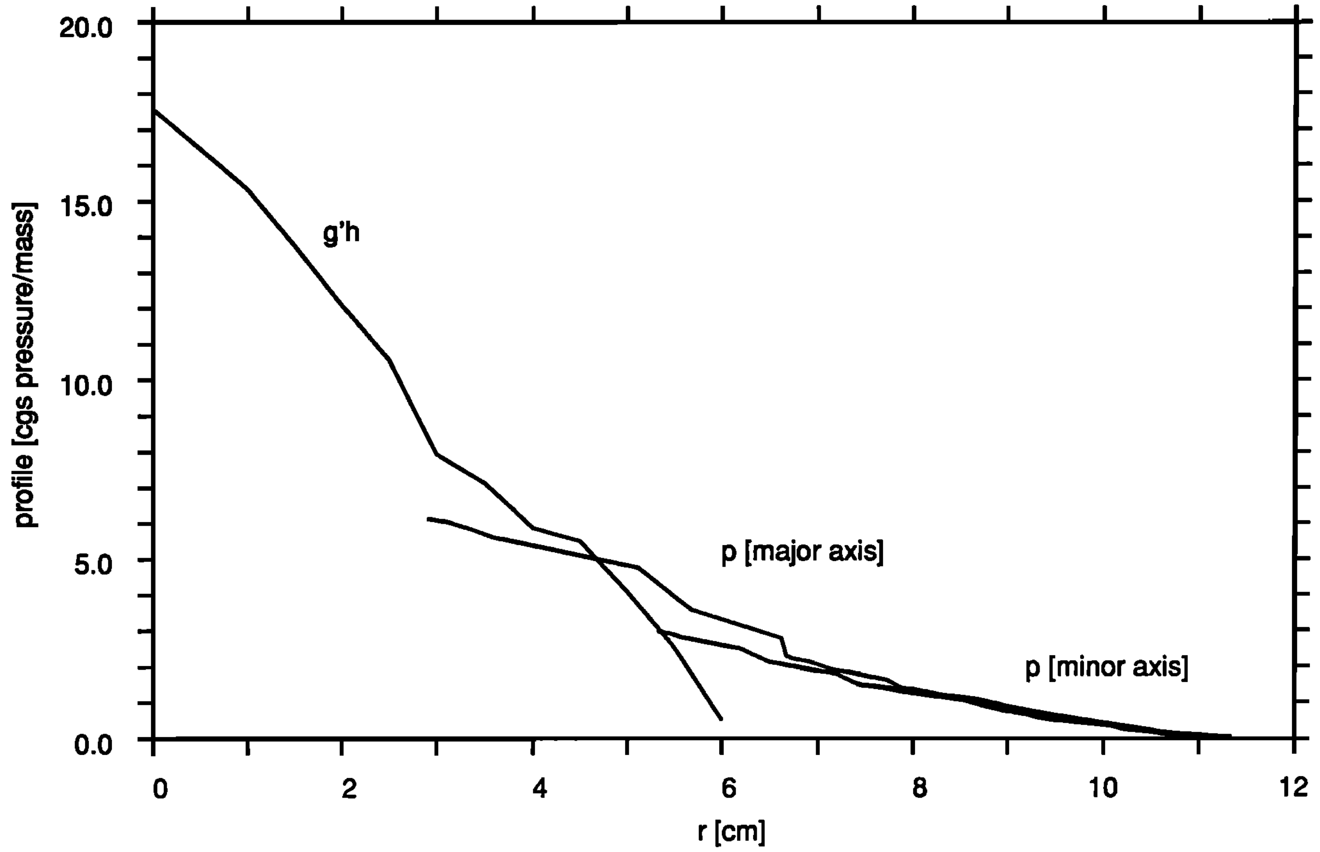

Fig. 25. Plot of p_1 and g^*h as functions of r for the second plume-generated eddy.

$$\underset{\sim}{u}_{2t} + \underset{\sim}{u}_2 \cdot \nabla\ \underset{\sim}{u}_2 + f\,\hat{k} \times \underset{\sim}{u}_2 = -\nabla p_2 \tag{6}$$

$$h_t + \nabla \cdot \underset{\sim}{u}_2\, h = 0 \tag{7}$$

$$p_2 = p_1 + g^*\, h + g^*\, Sy \tag{8}$$

where $\underset{\sim}{u}_1$ is the horizontal velocity of the horizontal upper fluid, $\underset{\sim}{u}_2$ is the velocity of the lower fluid, H is the mean fluid depth, h is the thickness of the lower layer blob, and is S is the slope of the bottom (g^* and other terms have already been defined); p_1 and p_2 represent the horizontally varying part of the dynamic pressure.

Integral Balances

Following *Ball* [1963] and *Killworth* [1979], we consider the moments for the lower layer continuity and momentum equations. From the lower layer mass equation (7), we have

$$\frac{\partial}{\partial t} \iint h\, dxdy = 0 \tag{9}$$

so that

$$V = \iint h\, dxdy \tag{10}$$

is constant. The x and y moments of mass equation are likewise simple

$$\dot{X} = \langle u_2\, h \rangle\ , \quad \dot{Y} = \langle v_2\, h \rangle \tag{11}$$

where

$$X \equiv \langle x\, h \rangle \text{ and } Y \equiv \langle yh \rangle \tag{12}$$

with the averaging operator defined by

$$\langle \phi \rangle = \frac{1}{V} \iint \phi\, dxdy \tag{13}$$

From the momentum equations (6) for layer 2 multiplied by h,

$$(h\, \underset{\sim}{u}_2)_t + \nabla \cdot (h\, \underset{\sim}{u}_2 \cdot \underset{\sim}{u}_2) + f\, \hat{k} \times h\, \underset{\sim}{u}_2 = -h \nabla p_2 \tag{14}$$

we find the integrated force balance

$$\begin{aligned} \ddot{\underset{\sim}{X}} + f\,\hat{k} \times \dot{\underset{\sim}{X}} &= -\langle h \nabla p_2 \rangle \\ &= -\langle h(\nabla p_1 + g^* \nabla h + g^* S\hat{y}) \rangle \\ &= -\langle h \nabla p_1 \rangle - g^* S\hat{y} \end{aligned} \tag{15}$$

after substitution from equation (8), where $\hat{x}$ and $\hat{y}$, are unit vectors in the x and y directions, respectively. When the frequency of centroid motion is low compared to f, we can balance the net Coriolis forces with the downslope gravitational force and the pressure forces from the upper layer

$$\underset{\sim}{\dot{X}} = \frac{1}{f}\,\hat{k} \times \langle h\,\nabla\,p_1\rangle - \frac{g^*S}{f}\,\hat{x} \tag{16}$$

As *Mory et al.* [1987] point out, this result implies that the blob will move at the Nof speed,

$$\underset{\sim}{\dot{X}} = -\frac{g^*S}{f}\,\hat{x} \tag{17}$$

if either (1) the upper layer pressure is sufficiently weak $|\,p_1\,| << g^*SL$ (where L is the eddy length scale) or (2) the upper layer pressure gradient fields are orthogonal to the bump topography. Thus if p_1 and h are both radially symmetric (or the contours are parallel) to suitable order, we still find the eddy moves at speed $-(g^*S/f)\,\hat{x}$. The speed, then, does not discriminate between the role of the upper layer, since the same propagation speed is found for eddies with predominantly lower layer circulation (the Nof case) and for those with primarily upper layer circulation, i.e., nearly compensated ($p_1 \cong -g^*h$) states. Both will yield the same translation rate.

Integral balances for the upper layer are less straightforward because of the contributions from the far field. The mass balance from integrating (5) is

$$\frac{\partial}{\partial t}\iint h\,dx\,dy = \oint \underset{\sim}{u}_1 \cdot \hat{n}\,(H - Sy) \tag{18}$$

where the integral is taken over some area larger than that occupied by the blob and $\hat{n}$ is the outward unit normal. But outside of the blob, the flow of the upper layer (the only layer present) is determined by a stream function

$$\underset{\sim}{u}_1\,(H - Sy) = \hat{k} \times \nabla\psi \tag{19}$$

so that we still find $\partial/\partial t \iint h\,dx\,dy = 0$. The expression derived from the first moment of the mass equation (5) becomes

$$\underset{\sim}{\dot{X}} = -\langle\,\underset{\sim}{u}_1\,(H - h - Sy)\rangle - \frac{1}{V}\oint \underset{\sim}{x}\,\nabla\,\psi \cdot \hat{t} \tag{20}$$

with $\underset{\sim}{X}$ being defined as before in equations (12) and $\hat{t}$ being the unit tangent vector to the curve bounding the area of integration. The momentum balance then yields

$$\underset{\sim}{\ddot{X}} + f\,\hat{k}\times\,\underset{\sim}{\dot{X}} = -\langle h\,\nabla\,p_1\rangle + \langle p_1\rangle\,S\hat{y} + \underset{\sim}{BT} \tag{21}$$

where $\underset{\sim}{BT}$ signifies the boundary terms from the integrals around the outer edge of the area of integration (again this is presumed to be larger than the blob). These terms are

$$\begin{aligned}\underset{\sim}{BT} = &-\tfrac{1}{V}\oint\,\underset{\sim}{x}\,\nabla\,\psi_t\,\cdot\hat{t} + \underset{\sim}{u}_1\,\nabla\,\psi\,\cdot\,\hat{t}\\ &+ f\,\hat{k}\times\,\underset{\sim}{x}\,\nabla\,\psi\,\cdot\,\hat{t} - (H - Sy)p_1\,\hat{x}\,\cdot\,\hat{n}\end{aligned} \tag{22}$$

Again looking at the low-frequency case of (21), dropping the $\underset{\sim}{\ddot{X}}$, we have

$$\underset{\sim}{\dot{X}} = \frac{1}{f}\,\hat{k}\times\langle h\,\nabla\,p_1\rangle + \frac{\langle p_1\rangle\,S}{f}\,\hat{x} - \frac{1}{f}\,\hat{k}\times\,\underset{\sim}{BT} \tag{23}$$

Combining (16) and (23), we find

$$\langle p_1\rangle\,\hat{x} = -g^*\,\hat{x} + \frac{1}{S}\,\hat{k}\times\,\underset{\sim}{BT} \tag{24}$$

We then obtain *Mory*'s [1985] result: if the eddy is isolated in the upper layer also, $|\,\underset{\sim}{BT}\,| << g^*S$, there must be a net cyclonic circulation in the upper layer of size

$$\langle p_1\rangle = -g^* \tag{25}$$

so that

$$\int_{-\infty}^{\infty}\int_{-\infty}^{\infty}(p_1 + g^*h)\,dx\,dy = 0 \tag{26}$$

On the average, then, if the flows in the upper layer decay rapidly enough away from the eddy in the radial direction, the lower layer blob is supported by a cyclonic low pressure above it in the upper region rather than by anticyclonic flows in the heavier fluid.

Scaled Equations

Let us now investigate more detailed models to study the conditions under which (26) applies. We nondimensionalize the equations as follows: x and y will be scaled by L, h by h_o, time by fL/g^*S (length divided by the characteristic propagation rate), lower layer velocities by g^*S/f, and upper layer velocities by $\alpha\,fh_oL/H$, with the pressure scales chosen by fL times velocity scale. The parameter α is a dimensionless number to be defined below. The upper layer velocity is chosen to balance vortex stretching with relative vorticity changes in the upper layer if $\alpha = 1$. For other balances we will choose different α values; e.g., (26) would predict $\alpha = g^*H/f^2L^2$. The nondimensional equations are

$$\beta\gamma^2\,\underset{\sim}{u}_{1_t} + \delta\,\alpha\,\underset{\sim}{u}_1\,\cdot\,\nabla\,\underset{\sim}{u}_1 + \hat{k}\,\times\,\underset{\sim}{u}_1 = -\nabla p_1 \tag{27}$$

$$-\frac{\beta\gamma^2}{\alpha}\,h_t + \nabla\,\cdot\,\underset{\sim}{u}_1\,(1 - \delta\,h - \beta\delta y) = 0 \tag{28}$$

$$\beta\gamma^2\,(\,\underset{\sim}{u}_{2_t} + \underset{\sim}{u}_2\,\cdot\,\nabla\,\underset{\sim}{u}_2) + \hat{k}\times\,\underset{\sim}{u}_2 = -\nabla\,p_2 \tag{29}$$

$$h_t + \nabla\,\cdot\,\underset{\sim}{u}_2\,h = 0 \tag{30}$$

$$\alpha\delta\,p_1 = \gamma^2\,\beta\,p_2 - \gamma^2\,h - \gamma^2\,\beta y \tag{31}$$

with the parameters being

$$\beta = \frac{SL}{h_o} \quad \delta = \frac{h_o}{H} \quad \gamma^2 = \frac{g^* h_o}{f^2 L^2} \quad \alpha = \frac{|\underset{\sim}{u}_1| H}{f h_o L} \tag{32}$$

β is the ratio of the topographic rise across the eddy to the eddy thickness, δ is the eddy thickness to the outer fluid depth, and γ is ratio of the deformation radius based on the denser fluid's thickness to the eddy size.

We shall consider three different parameter regimes:

1. Nof's Regime: For this case (deep upper layer) we have $\beta \sim \gamma^2 \sim 1$, $\delta << 1$ and $\alpha = 1$. At the lowest order, the lower layer is decoupled from the upper layer, and, as Nof proved, there exists a solution with a radially symmetric blob propagating westward at the nondimensional speed -1 ($c = -g^* S/f$). The upper layer responds weakly to the vortex stretching produced by the motion of the bump. In this regime, the upper layer motion cannot be strictly isolated since the nondimensional form of (26)

$$\alpha\,\delta \iint p_1 \, dx dy = -\gamma^2 \iint h \, dx dy \tag{33}$$

does not hold when $\delta << 1$.

2. Quasi-geostrophic regime: For the next case (large-scale eddies — $L \sim \sqrt{g^* H}/f$ rather than $\sqrt{g^* h_o}/f$ — and deep upper layer), we take $\beta \sim 1$, $\delta \sim \gamma^2 << 1$ and $\alpha = 1$. We can then use the standard quasi-geostrophic expansion for the upper layer to find

$$\begin{aligned} &\left[\frac{\partial}{\partial t} + \frac{\delta}{\beta\gamma^2}\left(\frac{\partial p_1}{\partial x}\frac{\partial}{\partial y} - \frac{\partial p_1}{\partial y}\frac{\partial}{\partial x}\right)\right] \\ &\left[\nabla^2 p_1 + h + \beta y\right] = 0 \end{aligned} \tag{34}$$

while the lower layer equations follow from the geostrophic and mass balance equations

$$\begin{aligned} h_t &+ \nabla \cdot \left[(\hat{k} \times \nabla p_2) h\right] = 0 \\ \Rightarrow h_t &+ J(p_2, h) = 0 \end{aligned} \tag{35}$$

Upon substitution of the hydrostatic relationship (31), we get finally

$$h_t - h_x + \frac{\delta}{\gamma^2 \beta} J(p_1, h) = 0 \tag{36}$$

We shall study the system of equations (34) and (36) analytically and numerically below: here we note only that it may be possible to find isolated solutions since the terms in (33) are the same order.

3. More nonlinear upper layers: The parameter regime which seems best fitted to the experiments is $\gamma^2 \sim 1$, $\delta \sim \beta < 1$; in addition, we choose $\alpha = \gamma^2/\delta$ to maintain a balance in the hydrostatic equation (and so that (33) may apply). This scaling has two problems : first, none of the parameters are very small, so that it is probably necessary to solve the full set; and second, even if we do assume that the parameters δ and β are both small enough to use as expansion parameters, the balances are not straightforward, since the upper layer momentum equation is fully nonlinear (though steady) at the first order. We have not carried this line of investigation further.

Quasigeostrophic Model Results

Consider the case of steadily moving eddies translating at speed c. For these, the dimensional forms of equations (34) and (36) become

$$\nabla^2 \psi_1 + \frac{f}{H}(h + Sy) = F(\psi_1 + cy) \tag{37}$$

$$h = G\left(\psi_1 + cy + \frac{g^* S}{f} y\right) \tag{38}$$

where F, G are arbitrary functions and the geostrophic pressure has been replaced by the stream function $\psi_1 = p_1/f$. For streamlines $\psi_1 + cy$ extending to ∞, we have

$$\nabla^2 \psi_1 + \frac{f}{H} h + \frac{f}{H} Sy = \frac{fS}{cH}(\psi_1 + cy) \tag{39}$$

so that

$$\nabla^2 \psi_1 - \frac{fS}{cH}\psi_1 = -\frac{f}{H} h \tag{40}$$

Since $c < 0$, the operator on ψ_1 has wavelike solutions, not trapped ones. Therefore to ensure isolated upper layer solutions, we need to have $\psi_1 = 0$ in regions where $h = 0$. Equation (38) applied where $h = 0$ then implies

$$G\left(cy + \frac{g^* S}{f} y\right) = 0 \tag{41}$$

This forces G and therefore h to be zero everywhere unless $c = -g^* S/f$. Thus the eddy must move with the Nof speed. We then find that (36) becomes

$$h = G(\psi_1) \tag{42}$$

and (40) becomes a (possibly) nonlinear equation for ψ_1. If we adopt the simple view that F is an analytic function and apply the modified form of (40),

$$\nabla^2 \psi_1 + \frac{f^2}{g^* H}\psi_1 = -\frac{f}{H} h \tag{43}$$

throughout space, we can prove that

$$\psi_1 = 0 \qquad h = 0 \tag{44}$$

if

$$\iint h(r,\theta)\, J_n\left(\frac{f}{\sqrt{g^* H}} r\right) e^{in\theta}\, r\, dr\, d\theta = 0 \tag{45}$$

for all n. In particular, from the $n = 0$ case, we see that h must be nonzero beyond a radius

$$r > 2.4\,\frac{\sqrt{g^* H}}{f} \tag{46}$$

where 2.4 is the first zero of J_o. Solutions with various test

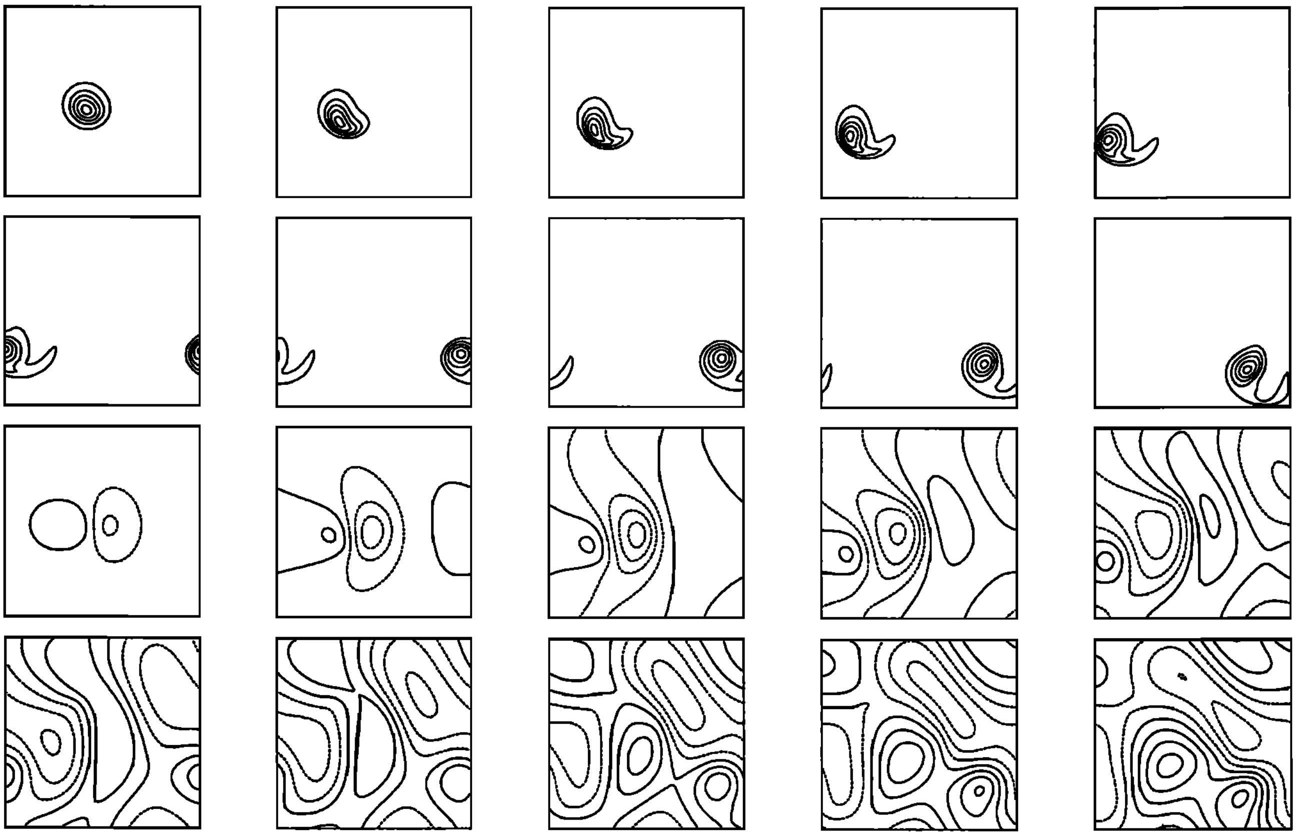

Fig. 26. Numerical solutions showing (top 10 panels) the evolution of the lower layer thickness at time $t = 1, 2, \ldots, 10$ (reading left to right) and (bottom 10 panels) upper layer pressure p_1 at the same time points. Contours are $\pm$ 0.1, $\pm$ 0.3, $\pm$ 0.5 ... (negative contours are dashed). The value of the ratio of bottom slope to eddy interface slope β is 0.23, and the nonlinearity parameter $q = \delta/\beta\gamma^2$ is 2.4. The initial pressure (hence initial motion) in the upper layer is 0.

functions for $h(r)$ suggest that the constant multiplier is usually considerably larger: e.g., for $h = h_0[1-(r/r_0)^2]$, the constant is 5.1 rather than 2.4. Thus we confirm Mory's result that the only equilibrium solutions are large compared to the deformation radius especially since the latter is usually based on the maximum blob thickness, h_o,

$$r > 2.4 \sqrt{\frac{H}{h_o}} \frac{\sqrt{g^* h_o}}{f} \tag{47}$$

The experiments clearly indicate a much smaller radius $r \approx 0.8 \sqrt{g^* H}/f$; while it may be possible that (37) and (38) have a solution with a nonanalytic functional F which has $r \sim \sqrt{g^* h_o}/f$, we have not found any and suspect that no such solution exists. Nonanalytical or time-dependent solutions are candidates for laboratory observation.

Numerical Experiments

We have solved (34) and (36) numerically for various choices of values for the parameters $q = \delta/\beta\gamma^2$ and β with $h(0) = \exp(-r^2)$ and $p_1(0) = p_1(0,0)\exp(-kr)^2$. A pseudospectral 64 × 64 code was used. The model is doubly periodic so that Rossby waves can propagate across the domain and return to influence the eddy. This problem is more severe in the cases where the upper layer is shallow. In Figures 26–30 the parameters β and q were set as close to the laboratory values as possible and the upper layer pressure factor A was systematically made more negative, starting from zero. For zero initial upper layer pressure (Figure 26), the bottom eddy slumped to the southwest and a radiated wave field was generated overhead and spread out relatively evenly over the entire domain. There is a high pressure center over the bottom eddy with a strong low pressure area behind. Figure 27 contains the results when the initial pressure field exactly satisfies the integral constraint $\delta \iint p_1 \, dx dy = \gamma^2 \iint h \, dx dy$ (equation (33)). The bottom material breaks into two blobs. One drifts slowly northwestward. The other, smaller fragment drifts southwest at roughly the Nof speed. The low pressure in the top fluid remains principally over the northern eddy, but still spreads out a little bit. Figure 28 shows the effect of a half-strength pressure field. The bottom material still breaks into two blobs, but they now have roughly equal volumes. The upper layer remains associated with the northern blob, but a stronger radiation pattern, like that in Figure 26, develops. The radiation is best illustrated by a nearly linear calculation in which the blob height is increased by a factor of 100 (Figure 29). The nonlinear terms are negligible so that (7.33) implies that the blob propagates smoothly at the Nof speed. This moving topography generates the upper layer wake pattern.

The association of an upper layer high-pressure center with the blob when the initial pressure field is zero is best

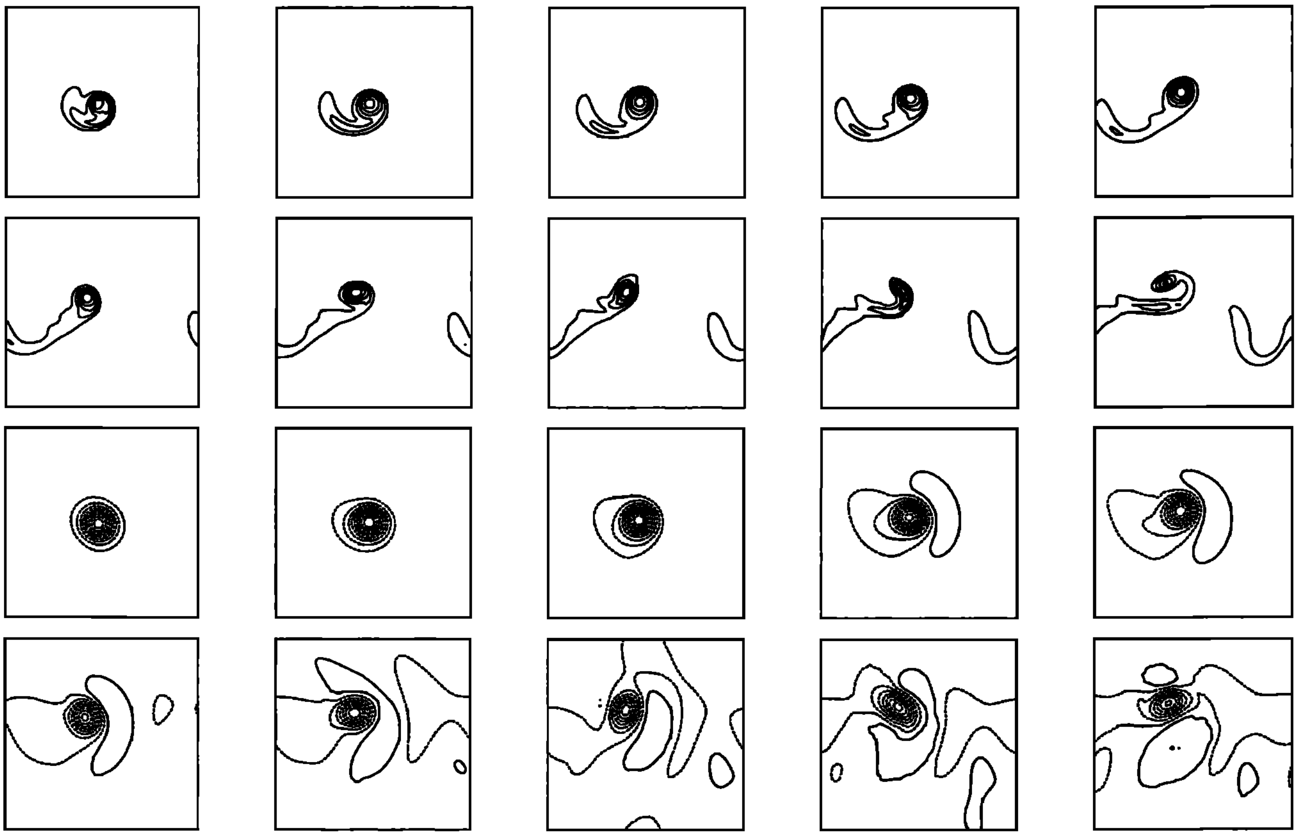

Fig. 27. Same as Figure 26 with initial pressure $p_1 = -1.81 \exp(-r^2)$, which satisfies the integral constraint given by equation (26).

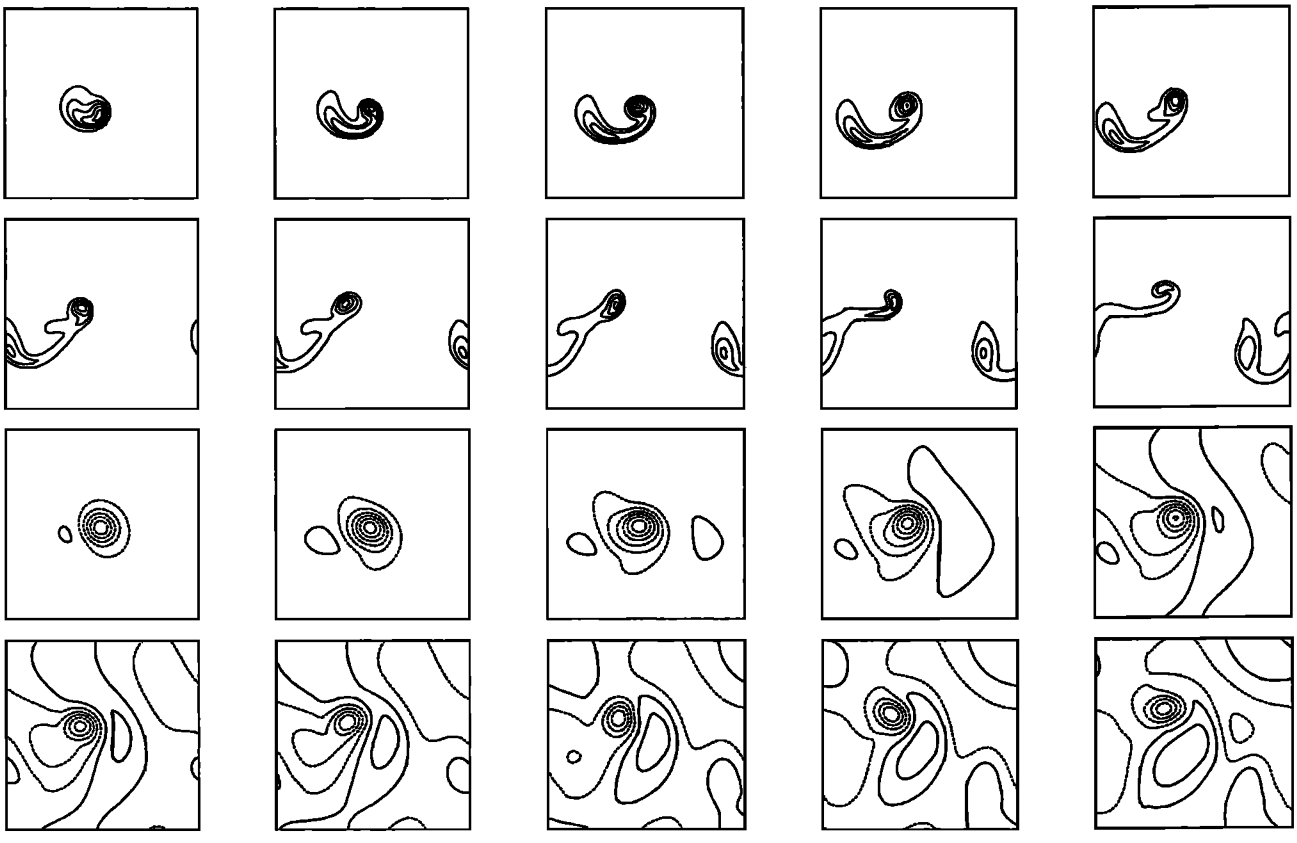

Fig. 28. Same as Figure 26 with initial pressure $p_1 = -0.905 \exp(-r^2)$, half that required for (26).

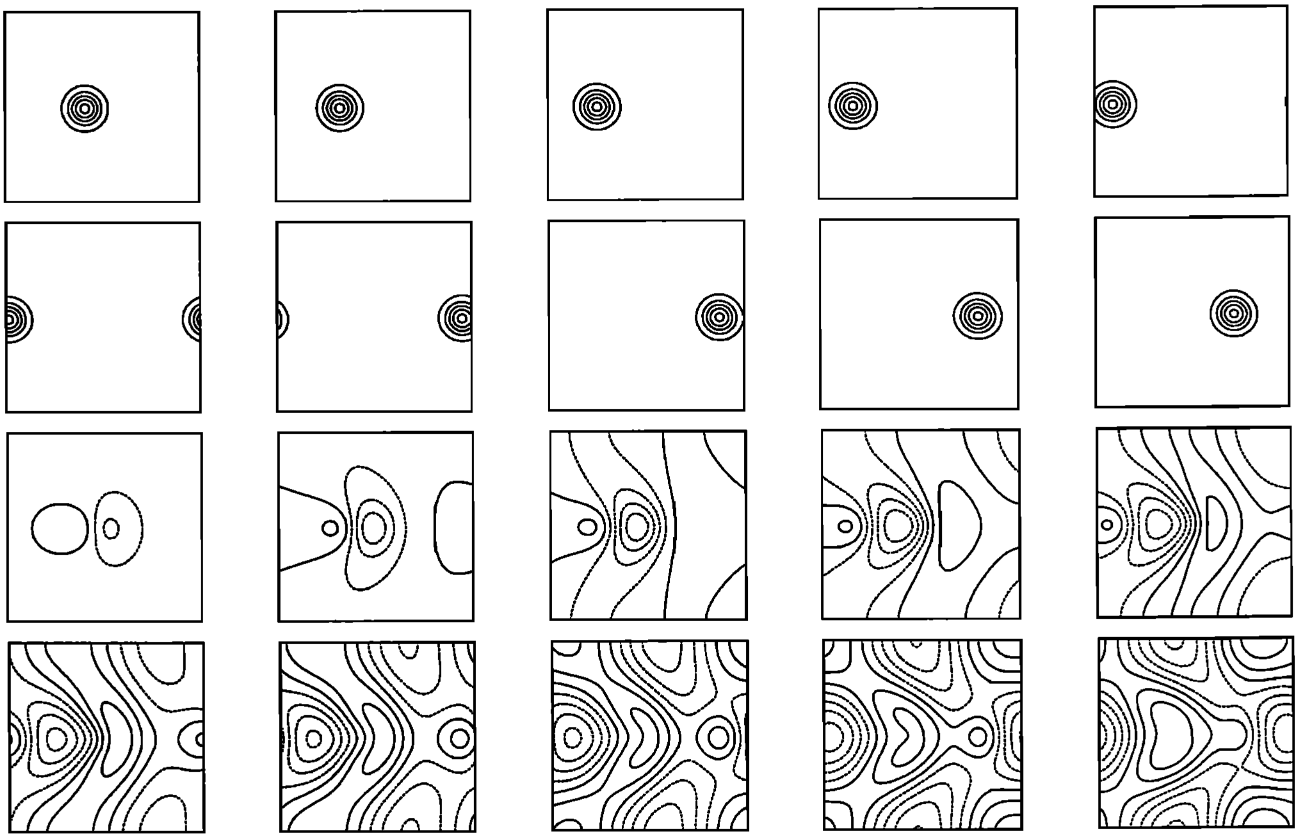

Fig. 29. A experiment in the more linear regime, $\beta = 23.0$, $q = 0.024$, showing the propagation at the Nof speed and the generation of a wake in the upper layer. This choice of parameters corresponds to keeping the values of g^*, H, L, fixed and letting h_0 become small. Note similarities to Figure 26 in Rossby wave patterns in the upper layer.

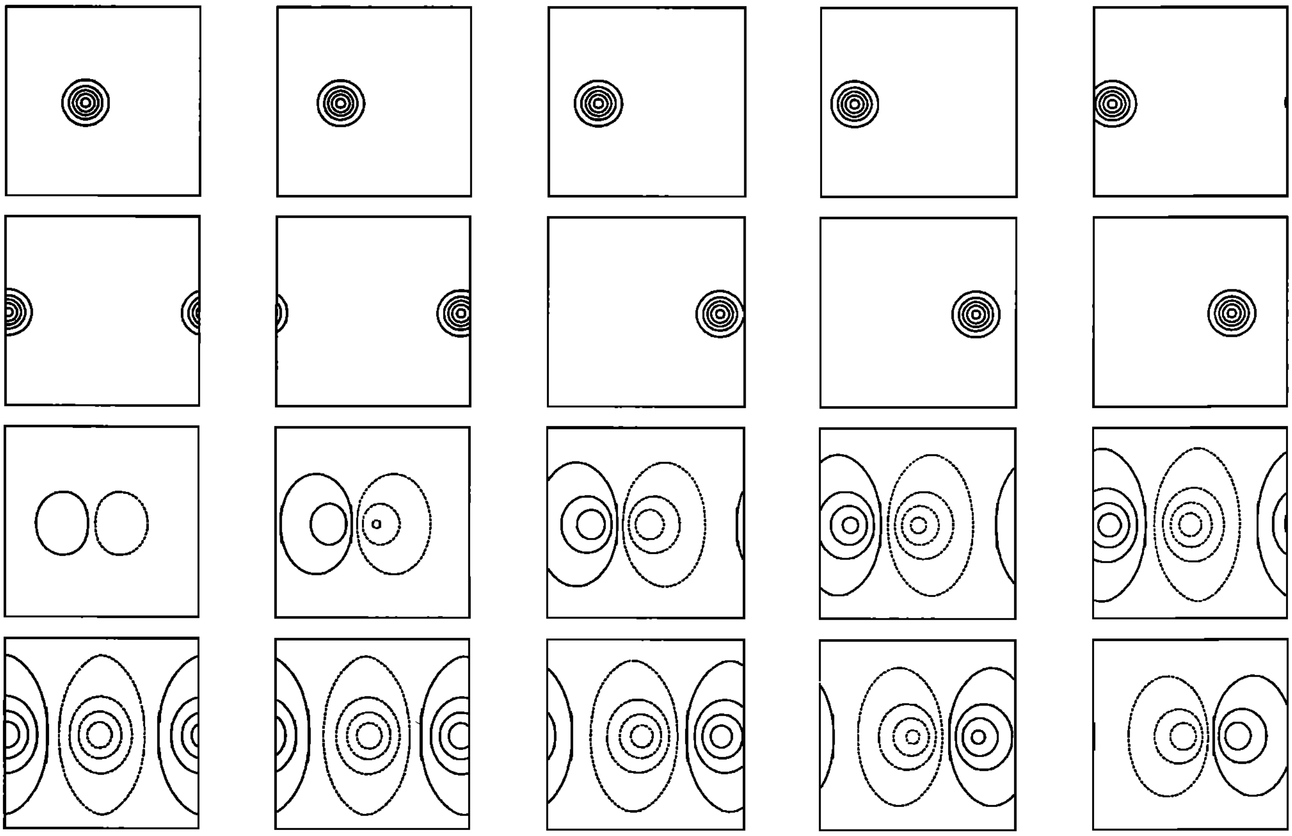

Fig. 30. An experiment with a deep upper layer, $\beta = 0.23$, $q = 0$.

illustrated by the case when the upper layer is very deep (Figure 30). The westward drift of the blob compresses upper layer fluid on its leading edge, generating anticyclonic vorticity, on top of the blob. The fluid which started at rest over the blob is stretched as the blob moves out from under, so that a cyclone is left at the origin.

These calculations reveal the difficulty of quasi-geostrophic equations reproducing the features of the laboratory eddies. Presumably, a more ambitious project using the primitive equations could replicate the laboratory results more faithfully.

8. CONCLUSIONS

We conclude that well-formed eddies can be produced from rather general nondescript initial conditions. The lenses of salty water travel westward parallel to the slope of the bottom. There is order of magnitude agreement with the speed prediction of *Nof* [1983] and *Mory et al.* [1987], though the estimates of speed from the data have considerable scatter. In contrast to the earlier experiments of *Mory* [1983] and Mory et al., our eddies travelled due west with little or no south to north drift observed.

Despite the agreement with Nof's prediction for the propagation rate, we have not observed the Nof solution with negligible motion overhead. We always saw unambiguous cyclonic circulation over the eddies as shown in Figures 4, 5, and 10. Figure 5 shows the trajectory of a surface float in the fresh water over the eddy. The run, with parameters marked by the circle in Figure 6, had a typical well-formed eddy. Not only does this track show clear evidence of cyclonic circulation over the eddy and westward drift of the eddy, but it also shows that fluid over the eddy remains trapped in the cyclonic circulation for many cycles and many eddy displacements. These observations qualitatively support the idea that the integral constraint of Mory et al. (equations 2 and 26), which requires cyclonic circulation over the eddy, is realized. Calculations show that the integral of the upper layer pressure can balance g^* times the volume of the lens, though the errors in the calculation are large. Dynamically, the integral balance implies that the thermal wind balance is satisfied on average by a jump from cyclonic upper layer velocities to nearly zero velocities in the lens. Our observations likewise bear this out: we see westward drift within the eddy, with the only circulating part being a weak cyclone rather than anticyclone. This does not mean that it is impossible to have anticyclonic eddies on a sloping bottom with only weak, nonisolated flows above; we simple have not seen such. Possibly, for example, the fluid was not deep enough to admit slow flows in the surface layer (indeed the Rossby number of the upper layer fluid was nearly one), the bottom fluid must be injected with more anticyclonic vorticity, or the friction must be reduced. However, the various methods we used to produce eddies all resulted in cyclonic upper layer supporting a relatively stagnant lens of salty fluid.

Theoretical constraints for a two-layer system show that the Nof speed g^*S/f is indeed appropriate if either the upper layer pressure is weak or is parallel to the contours of lens thickness. The first case (Nof's limit), while giving the proper translation speed, is not consistent with the flow fields observed. But attempts to find steady state solutions with upper layer cyclonic circulation give lens radii much larger than observed. Time-dependent quasi-geostrophic evolution experiments show much more distortion of the lens and stronger north-south translation than observed, though the details are sensitive to the initial upper layer pressure field. Also, the order one Rossby number in the upper layer makes the quasi-geostrophic assumption suspect. Thus while we are forced to consider upper layer motions as an essential part of the dynamics, we do not yet have a satisfactory model for them.

There is no clear evidence that the eddies can be represented as finite-amplitude waves. Rossby (topographic) waves are not obvious in the observations, although there is considerable velocity in the region between the eddy and the coast. We did note that the set of eddies produced by a coastal jet looks like soliton packets in that the leading eddy is biggest, the next is smaller, etc. However, it seems unlikely that these problems can be linked with inverse scattering theory.

One of the clearest experimental observations is that the cyclonic circulation over the eddy is generated by entrainment of fresh water into the salty water by small-scale turbulence. The mixture then gets lost by sinking into the large lens of brine. The cyclonic swirl in the top fluid was produced by the sinking. It was clearly visible in all runs. Cyclogenesis due to entrainment could be an important process in the ocean.

The fact that there is a regime diagram for the production of eddies implies that eddies emerge from some general stability or bifurcation problem. The formulation of such problems have not yet been made, and the finite-amplitude solutions are even further off.

Acknowledgments. This research was supported by the Division of Ocean Sciences of the National Science Foundation under grants OCE 84-16100 and OCE 87-14842, and by the Office of Naval Research under contract N00014-87-K-0007, NR-83-004. Discussions with Gordon Swaters were extremely helpful in developing the theoretical sections. Photography and assistance in the laboratory was given by Robert E. Frazel, whom we thank. Woods Hole Oceanographic Institution contribution 7054.

REFERENCES

Ball, F. K., Some general theorems concerning the finite motion of a shallow rotating liquid lying on a paraboloid, *J. Fluid Mech.*, *6*, 240–256, 1963.

Boyd, J. P., Analytic approximations to the modon dispersion relation, *Dyn. Atmos. Oceans*, *6*, 97–101, 1981.

Chow, V. T., *Open Channel Hydraulics*, 680 pp., McGraw-Hill, New York, 1959.

Ellison, T. H., and J. S. Turner, Turbulent entrainment in stratified flows, *J. Fluid Mech.*, *6*, 423–448, 1959.

Flierl, G. R., Baroclinic solitary waves with radial symmetry, *Dyn. Atmos. Oceans*, *3*, 15–38, 1979*a*.

Flierl, G. R., Planetary solitary waves, *Polymode News*, *62*, Woods Hole Oceanogr. Inst., Woods Hole, Mass., 1979*b*.

Flierl, G. R., Rossby wave radiation from a strongly nonlinear warm eddy, *J. Phys. Oceangr.*, 14, 47–58, 1984.

Flierl, G. R., V. D. Larichev, J. C. McWilliams, and G. M. Reznik, The dynamics of baroclinic and barotropic solitary eddies, *Dyn. Atmos. Oceans*, *5*, 1–41, 1980.

Flierl, G. R., M. E. Stern, and J. A. Whitehead, The physical significance of modons: laboratory experiments and general constraints, *Dyn. Atmos. Oceans*, 7, 233–263, 1983.

Griffiths, R. W., Inertial wave drag and the production of intense vortices by turbulent gravity current with implications for the sinking of bottom waters. *Ocean Modelling*, *50*, pp. 9–12 plus figures, Dep. App. Math. and Theor. Phys., Univ. of Cambridge, Cambridge, England, 1983.

Killworth, P. D., On "Chimney formations in the ocean," *J. Phys. Oceangr.*, *9*, 531–554, 1979.

Larichev, V. D., and G. M. Reznik, Two-dimensional Rossby soliton: An exact solution, *Reports U.S.S.R. Academy of Sciences*, *231(5)*, 1976a.

Larichev, V. D., and G. M. Reznik, Strongly nonlinear two-dimensional isolated Rossby waves, *Okeanologia*, *16*, 547–550, 1976b.

Malanotte-Rizzoli, P., Planetary solitary waves in geophysical flows, *Adv. Geophys.*, *24*, 147–224, 1982.

Mory, M., Theory and experiment of isolated baroclinic vortices on a sloping bottom, 1983 summer study program in geophysical fluid dynamics report, Woods Hole Oceanogr. Inst. *Tech. Rep. WHOI-83-41*, Woods Hole, Mass., 1983.

Mory, M., Integral constraints on bottom and surface isolated eddies, *J. Phys. Oceangr.*, *15*, 1433–1438, 1985.

Mory, M., M. E. Stern, and R. W. Griffiths, Coherent baroclinic eddies on a sloping bottom, *J. Fluid Mech.*, *183*, 45–62, 1987.

Nof, D., The translation of isolated cold eddies on a sloping bottom. *Deep Sea Res.*, *30*, 171–182, 1983.

Stern, M. E., Minimal properties of planetary eddies, *J. Mar. Res.*, *33*, 1–13, 1975.

Zabusky, N. J., and J. C. McWilliams, A modulated point-vortex model for geostrophic beta plane dynamics, *Phys. Fluids*, *25*, 2175–2182, 1982.

G. R. Flierl and B. A. Klinger, Department of Earth, Atmospheric and Planetary Sciences, Massachusetts Institute of Technology, Cambridge, MA 02139.

M. E. Stern, Department of Oceanography, Florida State University, Tallahassee, FL 32306.

J. A. Whitehead, Physical Oceanography Department, Woods Hole Oceanographic Institution, Woods Hole, MA 02543.

(Received February 13, 1989;
accepted July 10, 1989.)